Georgia Southern University

Digital Commons@Georgia Southern

2011

HST Morphologies of z~2 Dust Obscured Galaxies II. Bump Sources

R. Shane Bussmann
University of Arizona

Arjun Day
National Optical Astronomy Observatory

Jennifer Lotz
National Optical Astronomy Observatory

Lee Armus
California Institute of Technology

Michael J. I. Brown
Monash University, Michael.Brown@monash.edu

See next page for additional authors

Follow this and additional works at: https://digitalcommons.georgiasouthern.edu/physics-facpubs

Part of the Physics Commons

Authors

R. Shane Bussmann, Arjun Day, Jennifer Lotz, Lee Armus, Michael J. I. Brown, Peter Eisenhardt, James L. Higdon, Sarah J.U. Higdon, Buell T. Januzzi, Emeric Le Floc'h, J. Melbourne, B. T. Soifer, and Daniel Weedman

HST MORPHOLOGIES OF $z \sim 2$ DUST-OBSCURED GALAXIES II: BUMP SOURCES

R. S. Bussmann[1], Arjun Dey[2], J. Lotz[2,3], L. Armus[4], M. J. I. Brown[6], V. Desai[4], P. Eisenhardt[7], J. Higdon[8], S. Higdon[8], B. T. Jannuzi[2], E. Le Floc'h[9], J. Melbourne[10], B. T. Soifer[4,10], D. Weedman[11]

ABSTRACT

We present *Hubble Space Telescope* (*HST*) imaging of 22 ultra-luminous infrared galaxies (ULIRGs) at $z \approx 2$ with extremely red $R - [24]$ colors (called dust-obscured galaxies, or DOGs) which have a local maximum in their spectral energy distribution (SED) at rest-frame 1.6μm associated with stellar emission. These sources, which we call "bump DOGs", have star-formation rates of $400-4000\,M_\odot\,\mathrm{yr}^{-1}$ and have redshifts derived from mid-IR spectra which show strong polycyclic aromatic hydrocarbon emission — a sign of vigorous on-going star-formation. Using a uniform morphological analysis, we look for quantifiable differences between bump DOGs, power-law DOGs (*Spitzer*-selected ULIRGs with mid-IR SEDs dominated by a power-law and spectral features that are more typical of obscured active galactic nuclei than starbursts), sub-millimeter selected galaxies (SMGs), and other less-reddened ULIRGs from the *Spitzer* extragalactic First Look Survey (XFLS). Bump DOGs are larger than power-law DOGs (median Petrosian radius of 8.4 ± 2.7 kpc vs. 5.5 ± 2.3 kpc) and exhibit more diffuse and irregular morphologies (median M_{20} of -1.08 ± 0.05 vs. -1.48 ± 0.05). These trends are qualitatively consistent with expectations from simulations of major mergers in which merging systems during the peak star-formation rate period evolve from $M_{20} = -1.0$ to $M_{20} = -1.7$. Less obscured ULIRGs (i.e., non-DOGs) tend to have more regular, centrally peaked, single-object morphologies rather than diffuse and irregular morphologies. This distinction in morphologies may imply that less obscured ULIRGs sample the merger near the end of the peak star-formation rate period. Alternatively, it may indicate that the intense star-formation in these less-obscured ULIRGs is not the result of a recent major merger.

Subject headings: galaxies: evolution — galaxies: fundamental parameters — galaxies: high-redshift

1. INTRODUCTION

The discovery of a strong correlation between the stellar bulge mass and the central super-massive black hole (SMBH) mass of galaxies (e.g., Magorrian et al. 1998) has led to detailed theoretical models in which the growth of SMBHs and their host galaxies occur (nearly) simultaneously during a brief period of intense, merger-driven activity (e.g., Hopkins et al. 2006). In these models, the nature of the connection between SMBHs and their host galaxies has important implications for the evolution of massive galaxies.

The observational foundation of this evolutionary link between SMBHs and their host galaxies was established by studies of ultra-luminous infrared galaxies (ULIRGs) identified in the local universe using *InfraRed Astronomical Satellite* (see, e.g., Neugebauer et al. 1984; Sanders

& Mirabel 1996) data. ULIRGs are systems whose spectral energy distributions (SEDs) are dominated by dust emission at infrared (IR) wavelengths (Soifer et al. 1986) and whose morphologies tend to show evidence for recent or on-going major merger activity that has been linked to the formation of active galactic nuclei (AGN) and quasars (Sanders et al. 1988a). Although ULIRGs in the local universe are too rare to contribute significantly to the bolometric luminosity density, recent studies with the *Spitzer Space Telescope* have shown that they become increasingly important at higher redshifts (e.g. Le Floc'h et al. 2005; Magnelli et al. 2009). To understand the physical mechanisms that drive massive galaxy evolution, it is essential to identify and study high-redshift ($z > 1$), dusty, luminous galaxies that show signs of concurrent AGN and starburst activity.

Efforts to identify high-redshift ULIRGs have been increasingly fruitful over the last two decades. In particular, blank-field surveys at sub-millimeter or millimeter wavelengths have identified dusty and rapidly star-forming galaxies, the so-called sub-millimeter galaxies (SMGs; e.g. Smail et al. 1997; Coppin et al. 2006). More recently, the advent of the Multiband Imaging Photometer for Spitzer (MIPS; Rieke et al. 2004) on board the *Spitzer Space Telescope* has allowed for the identification of sources which are bright at mid-IR wavelengths but faint in the optical (e.g. Yan et al. 2004; Fiore et al. 2008; Dey et al. 2008; Lonsdale et al. 2009). Follow-up spectroscopy and clustering measurements of both the sub-millimeter-selected and the *Spitzer*-selected populations has demonstrated that they have similar number densities, redshift distributions, and clustering properties

[1] Steward Observatory, Department of Astronomy, University of Arizona, 933 N. Cherry Ave., Tucson, AZ 85721; rsbussmann@as.arizona.edu
[2] National Optical Astronomy Observatory, 950 N. Cherry Ave., Tucson, AZ 85719
[3] NOAO Leo Goldberg Fellow
[4] Spitzer Science Center, California Institute of Technology, MS 220-6, Pasadena, CA 91125
[6] School of Physics, Monash University, Clayton, Victoria 3800, Australia
[7] Jet Propulsion Laboratory, California Institute of Technology, MC 169-327, 4800 Oak Grove Drive, Pasadena, CA 91109
[8] Georgia Southern University, P.O. Box 8031, Statesboro, GA
[9] Laboratoire AIM-Paris-Saclay, CEA - CNRS -Universite Paris Diderot, CEA Saclay, Gif-sur-Yvette, 91191, FRANCE
[10] Caltech Optical Observatories, California Institute of Technology, Pasadena, CA 91125
[11] Astronomy Department, Cornell University, Ithaca, NY 14853

that indicate they are undergoing an extremely luminous, short-lived phase of stellar bulge and nuclear black hole growth and may be the progenitors of the most luminous ($\sim 4L^*$) present-day galaxies (Blain et al. 2004; Chapman et al. 2005; Yan et al. 2007; Farrah et al. 2006; Dey et al. 2008; Brodwin et al. 2008).

One intriguing difference between the the ULIRG samples selected at different wavelengths (as might be expected based on the selection criteria) is that the mid-IR selected ULIRGs have hotter dust than the far-IR selected SMGs (Kovács et al. 2006; Coppin et al. 2008; Sajina et al. 2008; Younger et al. 2009; Lonsdale et al. 2009; Bussmann et al. 2009a; Fiolet et al. 2009). This distinction may be analogous to the warm-dust/cool-dust dichotomy seen in local ULIRGs, where it has been suggested that warm ULIRGs represent an important transition stage between cold ULIRGs and quasars (Sanders et al. 1988b). Furthermore, the mid-IR-selected population shows a range of spectral energy distributions (SEDs), with the brighter sources showing power-law SEDs in the mid-IR ("power-law" sources), and the fainter ones exhibiting peaks at rest-frame wavelengths near 1.6μm (the "bump" sources). The bump is generally attributed to starlight and 1.2 mm photometry suggests that the "bump" sources are dominated by cooler dust than the power-law sources (Lutz et al. 2005; Sajina et al. 2008; Younger et al. 2009; Lonsdale et al. 2009; Bussmann et al. 2009a; Fiolet et al. 2009). (Lutz et al. 2005; Sajina et al. 2008; Younger et al. 2009; Lonsdale et al. 2009; Bussmann et al. 2009a; Fiolet et al. 2009). Also, the mid-IR spectra of bump sources show strong polycyclic aromatic hydrocarbon (PAH) emission features typical of star-forming regions (Yan et al. 2007; Desai et al. 2009; Huang et al. 2009), while power-law sources have silicate absorption features or are dominated by continuum emission consistent with obscured AGN (Houck et al. 2005; Weedman et al. 2006b; Yan et al. 2007). These results suggest that there may be a connection between the power source responsible for the bolometric luminosity of a system and its globally averaged dust temperature.

Efforts to understand this connection between mid-IR and far-IR selected high-z ULIRGs within the context of an evolutionary paradigm have been recently advanced by numerical simulations of galaxy mergers (e.g. Mihos & Hernquist 1996; Narayanan et al. 2009). In these models, when the merging system approaches final coalescence, the star-formation rate (SFR) spikes and, because it is enshrouded in cold-dust, the system is observed as an SMG. As time proceeds, feedback from the growth of a central super-massive black hole warms the ambient dust and ultimately quenches star-formation. It is during this critical period of galaxy evolution when the system is observable as a *Spitzer*-selected ULIRG. The models predict observable morphological differences between the various phases of the merger and, in particular, suggest that mergers occupy a distinct morphological phase space during the "final coalescence" period when the SFR peaks (Lotz et al. 2008, 2009b,a). To test these predictions, and in general to understand the physical processes governing galaxy evolution, it is essential to study the *Spitzer*-selected and SMG populations in detail.

We have embarked on a detailed study of a large sam-

ple of extremely dust-obscured, high-redshift ULIRGs with the goal of understanding their evolutionary history. Our sample is selected using *Spitzer* and ground-based optical imaging of the Boötes field of the NOAO Deep Wide-Field Survey (NDWFS[11]; Jannuzi et al., in prep.; Dey et al., in prep. Jannuzi & Dey 1999) to have extreme optical-to-mid-IR colors $R - [24] \geq 14$ Vega mag ($\approx F_\nu(24\mu m)/F_\nu(R) \geq 1000$) and are called Dust-Obscured Galaxies (DOGs). Spectroscopic redshifts for a subset of the DOGs have been measured using the Infrared Spectrometer (IRS; ?) on *Spitzer* and optical and near-IR spectrographs at the W. M. Keck Observatory (Houck et al. 2005; Weedman et al. 2006b; Desai et al. 2009). DOGs satisfying $F_\nu(24\mu m) \geq 0.3$ mJy have a fairly narrow distribution in redshift ($z \approx 2.0 \pm 0.5$) and a space density of $\approx 2.8 \times 10^{-5} h_{70}^3 \mathrm{Mpc}^{-3}$ (Dey et al. 2008). Although rare, these sources are sufficiently luminous that they contribute up to one-quarter of the total IR luminosity density at redshift $z \sim 2$ and constitute a substantial fraction of the ULIRG population at this redshift.

DOGs are the most dust-reddened ULIRGs at $z \approx 2$; similar to the broader ULIRG population, DOGs exhibit a wide range in SED stretching from power-law dominated mid-IR SEDs (i.e., "power-law DOGs") to SEDs which exhibit bumps (i.e, "bump DOGs"). In Bussmann et al. (2009b, hereafter Paper I), we analyzed the morphologies of 31 of the brightest 24μm-selected DOGs (all with $F_{24\mu m} > 0.8$ mJy) that have power-law mid-IR SEDs. All of these objects had spectroscopic redshifts and most exhibit strong 9.7μm silicate absorption in their IRS spectra (Houck et al. 2005; Weedman et al. 2006b; Desai et al. 2009). The power-law DOGs are nearly always spatially resolved, with effective radii of $1 - 5$ kpc, although a few show obvious signs of merger activity (Dasyra et al. 2008; Bussmann et al. 2009b). K-band adaptive optics imaging (from Keck) of 15 objects has revealed an intriguing dependence of size on SED shape: power-law dominated sources are more compact than 24μm-faint bump-dominated sources (Melbourne et al. 2008, 2009). This is consistent with the idea of the bright, power-law DOGs being more AGN dominated.

The primary goal of this paper is to identify any quantifiable morphological differences between SMGs, *Spitzer*-selected bump ULIRGs and other *Spitzer*-selected power-law ULIRGs. We present and analyze new *HST* Wide-Field Planetary Camera 2 (WFPC2 Trauger et al. 1994) and Near-IR Camera and Multi-object Spectrometer (NICMOS Thompson et al. 1998) observations of 19 bump DOGs and 3 more power-law DOGs. We also assemble a larger sample of $z \approx 2$ ULIRGs, drawn from Paper I (power-law DOGs) and the literature, with high spatial resolution imaging data appropriate for morphological analyses. In particular, we include a large sample of SMGs (from the stufy of Swinbank et al. 2010) and expand the sample of *Spitzer*-selected ULIRGs by including those from the eXtragalactic First Look Survey (XFLS; Dasyra et al. 2008). Our combined dataset contains 103 high-redshift ULIRGs with available and fairly comparable *HST* data. We present a uniform morphological analysis of these objects and compare the results to the expectations from models

---

[11] http://www.noao.edu/noaodeep

for the formation and evolution of these systems.

In section 2 we detail the sample selection, observations, and data reduction. In section 3, we describe our methodology for measuring photometry and morphologies, including a visual classification experiment, non-parametric quantities, and GALFIT modeling. Section 4 contains the results of this analysis, including a comparison of SMG, DOG, and simulated merger morphologies. In section 5, we discuss the implications of our results. We summarize our conclusions in section 6.

Throughout this paper we assume $H_0 = 70$ km s^{-1} Mpc^{-1}, $\Omega_m = 0.3$, and $\Omega_\lambda = 0.7$. At $z = 2$, this results in a spatial scale of 8.37 kpc/$''$.

2. DATA

In this section, we describe the new *HST* observations of bump DOGs and the procedure used to reduce them. We also detail the archival datasets of power-law DOGs, SMGs, and XFLS ULIRGs used in subsequent sections of this paper.

2.1. *Bump DOGs*

The 22 DOGs presented in this paper were observed with *HST* from 2007 December to 2008 May. All were observed with WFPC2 through the F814W filter and with the NICMOS NIC2 camera through the F160W filter. Table 1 summarizes the details of the observations. All data were processed using IRAF[12]. The following sections provide more details about the sample selection and processing of the WFPC2 and NICMOS images used in this paper.

2.1.1. *Sample Selection*

A sample of 2603 DOGs was identified by Dey et al. (2008) from the 9.3 deg^2 Boötes Field of the NDWFS. Keck and *Spitzer* spectroscopy have resulted in redshifts of $\approx$ 100 DOGs, approximately 60% of which have power-law dominated mid-IR SEDs and 40% have bump SEDs. These are objects which have very high intrinsic to observed UV luminosity ratios, on par with or beyond the most extreme starbursts studied by *Spitzer* in the local universe (Sargsyan et al. 2010).

In Bussmann et al. (2009b, hereafter Paper I), we analyzed *HST* imaging (program HST-GO10890) of 31 of the brightest DOGs at 24μm (all have $F_{24\mu m} > 0.8$ mJy) that have power-law mid-IR SEDs and spectroscopic redshifts based on the 9.7μm silicate absorption feature, most likely due to the presence of warm dust heated by an AGN (Weedman et al. 2006a; Donley et al. 2007; Polletta et al. 2008; Brand et al. 2008).

In this paper, we analyze *HST* imaging (program HST-GO11195) of 22 DOGs that show a bump in their rest-frame mid-IR SED (selected using Arp 220 as a template; for details see Desai et al. 2009). This feature indicates that the mid-IR light is dominated by stellar emission in these sources. Furthermore, *Spitzer* mid-IR spectroscopy has provided redshifts for 20/22 of these sources via identification of PAH emission features commonly associated with on-going star-formation (Desai et al. 2009). Subsequent deeper mid-IR imaging from the *Spitzer* Deep
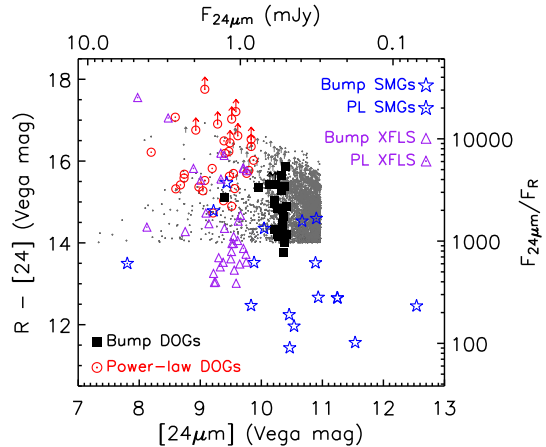
---

[12] IRAF is distributed by the National Optical Astronomy Observatory, which is operated by the Association of Universities for Research in Astronomy, Inc., under cooperative agreement with the National Science Foundation. http://iraf.noao.edu/

FIG. 1.— $R - [24]$ color vs. 24μm magnitude distribution for all DOGs in the NDWFS Boötes field (gray dots). Arrows indicate R-band non-detections (2σ level), and cross symbols highlight power-law dominated sources. Also shown are the samples with high-spatial resolution imaging studied in this paper: power-law DOGs (red circles), bump DOGs (black squares), SMGs (blue stars), and XFLS ULIRGs (purple triangles). Power-law sources tend to be the brightest at 24μm and the most heavily obscured.

Wide-Field Survey (Ashby et al. 2009) has revealed that the two sources lacking PAH features have power-law mid-IR SEDs. One additional target has a power-law mid-IR SED (SST24 J143028.5+343221) and was observed by *HST* because the bump source it replaced could not be observed due to scheduling constraints.

Figure 1 shows the $R - [24]$ color and R-band magnitude (Vega system) for the following sources with *HST* imaging: bump and power-law DOGs, SMGs, and XFLS ULIRGs at high redshift. Following careful reanalysis of the R-band photometry (compared to Dey et al. 2008, with the main difference being a revised estimate of the sky background level), a few DOGs show $R - [24]$ colors ≈ 0.1 mag below the nominal DOG threshold. We refer to these objects as DOGs in this paper because they satisfy the essential physical characteristics of DOGs: they are $z \sim 2$ ULIRGs that are likely to be a highly obscured stage in massive galaxy evolution. The bump DOGs in this sample have fainter 24μm flux densities and less extreme $R - [24]$ colors than the power-law DOGs. These distinctions are qualitatively representative of the photometric properties of the full sample of 2603 DOGs in the Boötes Field.

Figure 2 shows the redshift distributions of bump DOGs, power-law DOGs, SMGs, and XFLS ULIRGs with *HST* data in comparison to all DOGs in Boötes with spectroscopic redshifts. Bump DOGs predominantly lie in a relatively narrow redshift range of $1.5 < z < 2.1$. Briefly, this is because at $z = 1.9$, the strong 7.7μm PAH feature boosts the 24μm flux, pushing sources with weaker continuum into the flux-limited bump DOG sample (for additional details, see Desai et al. 2009).

2.1.2. *WFPC2 Data*

The Wide Field Camera CCD 3 of WFPC2 was used to image the 22 DOGs in this study. These observations consisted of double-orbit data with the F814W filter. We used a three point dither pattern (WFPC2-LINE) with a point and line spacing of 0$''$3535 and a pattern orientation of 45°. Total exposure duration at the nominal pixel

TABLE 1
OBSERVATIONS

Source Name	ID[a]	RA (J2000)	DEC (J2000)	z[b]	WFPC2/F814W	NIC2/F160W
SST24 J142637.3+333025	1	+14:26:37.397	+33:30:25.82	3.200[c]	2008-02-11	2007-12-31
SST24 J142652.4+345504	12	+14:26:52.555	+34:55:05.53	1.91	2008-03-28	2008-01-01
SST24 J142724.9+350823	4	+14:27:25.016	+35:08:24.20	1.71	2008-07-02	2008-01-14
SST24 J142832.4+340850	8	+14:28:32.476	+34:08:51.23	1.84	2008-07-03	2008-01-15
SST24 J142920.1+333023	17	+14:29:20.164	+33:30:23.59	2.01	2008-02-01	2008-05-26[d]
SST24 J142941.0+340915	13	+14:29:41.085	+34:09:15.61	1.91	2008-05-21	2008-03-15
SST24 J142951.1+342041	5	+14:29:51.163	+34:20:41.33	1.76	2008-01-28	2008-01-14
SST24 J143020.4+330344	11	+14:30:20.537	+33:03:44.45	1.87	2008-03-21	2008-04-11
SST24 J143028.5+343221	21	+14:30:28.534	+34:32:21.62	2.178[e]	2008-05-07	2008-01-15
SST24 J143137.1+334500	7	+14:31:37.080	+33:45:01.26	1.77	2008-05-20	2008-04-12
SST24 J143143.3+324944	2	+14:31:43.400	+32:49:44.38	—	2008-02-10	2008-03-15
SST24 J143152.4+350029	3	+14:31:52.463	+35:00:29.44	1.50	2008-01-24	2008-05-22
SST24 J143216.8+335231	6	+14:32:16.904	+33:52:32.18	1.76	2008-02-01	2008-03-16
SST24 J143321.8+342502	18	+14:33:21.890	+34:25:02.62	2.10	2008-05-21	2008-01-15
SST24 J143324.2+334239	14	+14:33:24.269	+33:42:39.55	1.91	2008-02-02	2008-01-17
SST24 J143331.9+352027	15	+14:33:31.945	+35:20:27.28	1.91	2007-12-25	2008-01-14
SST24 J143349.5+334602	10	+14:33:49.585	+33:46:02.00	1.86	2008-03-18	2008-01-07
SST24 J143458.8+333437	20	+14:34:58.953	+33:34:37.57	2.13	2008-07-03	2008-05-21
SST24 J143502.9+342657	19	+14:35:02.930	+34:26:58.88	2.10	2008-05-09	2008-01-15
SST24 J143503.3+340243	16	+14:35:03.336	+34:02:44.16	1.97	2008-02-29	2008-01-07
SST24 J143702.0+344631	22	+14:37:02.018	+34:46:30.93	3.04	2008-03-28	2007-12-28
SST24 J143816.6+333700	9	+14:38:16.714	+33:37:00.94	1.84	2008-07-03	2008-01-14

[a] Panel number in Figure A1
[b] Redshift from *Spitzer*/IRS (Desai et al. 2009) unless otherwise noted
[c] Redshift from Keck LRIS (Soifer et al., in prep.)
[d] This observation provided no usable data
[e] Redshift from Keck NIRSPEC (Brand et al. 2007)

scale of $0''.1$ pix^{-1} was $\approx$3800 sec. The standard WFPC2 pipeline system was used to bias-subtract, dark-subtract, and flat-field the images (Mobasher et al., 2002). MultiDrizzle was then used to correct for geometric distortions, perform sky-subtraction, image registration, cosmic ray rejection and final drizzle combination (Koekemoer et al. 2002). We used a square interpolation kernel and output pixel scale of $0.075''$ pix^{-1}, leading to a per-pixel exposure time in the drizzled image of $\approx$2200 sec. Typically, a point source with an F814W AB magnitude of 26.1 may be detected at the 5σ level by using a $0''.3$ diameter aperture.

2.1.3. NICMOS Data

Single-orbit data of the DOGs were acquired with the NIC2 camera and the F160W filter. We used a two-
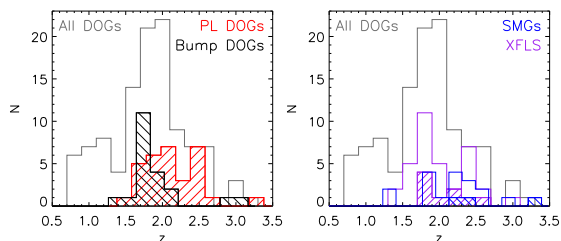

FIG. 2.— *Left*: Redshift distribution of DOGs in the Boötes Field with spectroscopic redshifts (gray histogram; either from *Spitzer/IRS* or Keck DEIMOS/LRIS, Soifer et al. in prep.). The hatched histograms show the redshift distributions of the subset of power-law DOGs (red) and bump DOGs (black) studied in this paper. The redshift distribution of bump DOGs is relatively narrow due to selection effects (for details see Desai et al. 2009), while power-law DOGs are weighted towards slightly larger redshifts. *Right*: Redshift distribution of SMGs (blue histogram) and XFLS ULIRGs (purple histogram) at $z > 1.4$ studied in this paper. Hatched regions denote the sub-sample qualifying as power-law dominated in the mid-IR.

point dither pattern (NIC-SPIRAL-DITH) with a point spacing of $0.637''$. The total exposure time per source was $\approx$2700 s.

We followed the standard data reduction process outlined in the NICMOS data handbook (Viana et al. 2009). We used the IRAF routine `nicpipe` to pre-process the data, followed by the `biaseq` task to correct for non-linear bias drifts and spatial bias jumps. We then used `nicpipe` a second time to do flat-fielding and initial cosmic-ray removal. The IRAF task `pedsky` was used to fit for the sky level and the quadrant-dependent residual bias. Significant residual background variation remained after this standard reduction process. To minimize these residuals, we followed the procedure outlined in Paper I: we constructed an object-masked median sky image based on all of our NIC2 science frames, scaled it by a spatially constant factor and subtracted it from each science image. The scaling factor was computed by minimizing the residual of the difference between the masked science image and the scaled sky image. Mosaicing of the dithered exposures was performed using `calnicb` in IRAF, resulting in a pixel scale of $0.075''$ pix^{-1}. Although the noise varies from image to image, typically a point source with an F160W AB magnitude of 25.2 may be detected at the 5σ level by using a $0''.3$ diameter aperture.

2.1.4. Astrometry

Each WFPC2 and NICMOS image is aligned to the reference frame of the NDWFS, which itself is tied to the USNO A-2 catalog. We identify well-detected, unsaturated sources in the *I*-band NDWFS data overlapping the field of view (FOV) of each WFPC2/F814W image using Source Extractor (SExtractor, version 2.5.0, Bertin & Arnouts 1996). The IRAF tasks `wcsctran` and

`imcentroid` are used to convert the RA and DEC values of this list of comparison sources into WFPC2 pixel coordinates. Finally, the IRAF task `ccmap` is used to apply a first order fit which corrects the zero point of the astrometry and updates the appropriate WCS information in the header of the WFPC2 image. The aligned WFPC2 image serves as a reference frame for correcting the astrometry of the NICMOS image as well as the IRAC images (since the IRAC images of the Boötes Field are not tied to the USNO A-2 catalog, but instead to the $2\mu m$ All-Sky Survey frames, see Ashby et al. 2009) using a similar procedure. The properly aligned, multi-wavelength dataset generally allows for straightforward identification of the proper counterpart to the MIPS source, since inspection of the four IRAC channels reveals a single source associated with the $24\mu m$ emission for all sources. The absolute uncertainty in the centroid of the IRAC $3.6\mu m$ emission ranges from $0\rlap{.}''2$-$0\rlap{.}''4$.

2.2. *Power-law DOGs*

In Paper I we analyzed *HST* imaging of 31 power-law DOGs at $z > 1.4$. Although these sources have mid-IR SED features indicative of obscured AGN, their rest-frame optical morphologies nearly all show minor ($< 30\%$) point-source contributions and significant emission on scales of 1-5 kpc. This indicates that the rest-frame optical light of these sources is produced from stars, rather than AGN.

The NICMOS exposure times and H-band luminosities of these sources are similar to the bump DOGs, facilitating a comparison between the two populations. This particular comparison — between distinct sub-classes of the most extreme dust-obscured ULIRGs — is a major aspect of this study.

2.3. *SMG Data*

The SMG data used in this paper are *HST* NICMOS/F160W imaging of a sample of 25 SMGs selected from a catalog of 73 SMGs with spectroscopic redshifts (Chapman et al. 2005) and were first presented by Swinbank et al. (2010). Of the 25 SMGs, 23 have single-orbit NIC2 imaging from Cycle 12 *HST* program GO-9856 (Swinbank et al. 2010) and an additional 6 have multi-orbit NIC3 imaging from GOODS-N (Conselice et al. 2010 in prep.). *HST* optical imaging in the F814W filter is also available for all of these objects.

In this paper, we focus on the subset of 18 SMGs at $z > 1.4$. Of these 18, all have NIC2 imaging and three (SMM J123622.65+621629.7, SMM J123632.61+620800.1, and SMM J123635.59+621424.1) have NIC3 imaging as well. Although the NIC3 images are significantly deeper, we prefer to use the NIC2 data (each of these sources is well-detected at S/N> 2) because of the superior pixel scale of NIC2 and the unusual shape of the NIC3 PSF. Some of these sources have optical *HST* imaging with the Advanced Camera for Surveys (ACS), but the S/N levels are generally insufficient for quantitative analysis and so are not used in this study.

We obtained the NIC2 images of SMGs from the *HST* data archive and reduced them following the same procedure that is outlined in section 2.1.3. Most importantly, the methodology used to analyze the photometry and morphology of both SMGs and DOGs in this study is identical and is described in section 3.

2.4. *XFLS Data*

A sample of 33 XFLS ULIRGs at $z > 1.4$ was imaged with *HST* NICMOS/F160W in Cycle 15 as part of program GO10858. These data and a morphological analysis of the imaging was presented in Dasyra et al. (2008). We note that in our study, we use only single-orbit NIC2 data of these objects to facilitate comparison with the NIC2 images of the other high-z ULIRG populations studied here, which all have only single-orbit NIC2 data. Double-orbit imaging is available for nearly 50% of the sample and in principle could be used to measure more accurate morphologies of the fainter objects as well as test for systematic errors in the morphologies resulting from low S/N. The data were obtained from the *HST* data archive, reduced, and analyzed using the same methodology that was applied to DOGs and SMGs.

3. METHODOLOGY

In this section, we describe our methods to measure photometry as well as visual, non-parametric, and GALFIT morphologies.

3.1. *Photometry*

We perform $2''$ diameter aperture photometry on each DOG in both the NICMOS and WFPC2 images, choosing the center of the aperture to be located at the peak flux pixel in the NICMOS images. Foreground and background objects are identified and removed using SExtractor (see Section 4.2.2). The sky level is derived using an annulus with an inner diameter of $2''$ and a width of $2''$. In cases where the flux density radial profile did not flatten at large radii, the appropriate sky value was determined by trial-and-error. Photometric uncertainty was computed by measuring the sigma-clipped root-mean-square of fluxes measured in N $2''$ diameter apertures, where $N \approx 10$ and $N \approx 100$ for the NICMOS and WFPC2 images, respectively. We verified the accuracy of our WFPC2 photometric zeropoints by comparing well-detected, non-saturated sources common to both the WFPC2/F814W and NDWFS/I-band imaging. Photometric measurements of the DOGs are presented in Table 2.

3.2. *Morphology*

To analyze the morphologies of the bump DOGs, we follow a similar procedure to that outlined in Paper I. Here we summarize the three different, complementary approaches used in analyzing the morphology of the DOGs in our sample: a visual classification experiment, multi-component GALFIT modeling, and non-parametric quantification.

3.2.1. *Visual Classification*

For this paper, our visual classification experiment differed significantly from Paper I. The goal of the original experiment outlined in Paper I was to determine if DOGs could be distinguished from normal field galaxies based on a visual classification. This proved difficult to quantify due to the faintness of DOGs in the rest-frame UV

(ACS/WFPC2 images) and the small number of field galaxies in the rest-frame optical (NICMOS images).

Our new classification experiment is designed specifically to identify morphological differences found in the NICMOS imaging of bump and power-law DOGs. We generated a 5″x5″ cutout image of every DOG with NICMOS data (both power-law and bump sources, a total of 53 objects) and arranged them randomly. Seven of the coauthors classified these objects into "Regular", "Irregular", or "Too Faint To Tell". In addition to probing for a difference between bump and power-law DOGs, the mode of the classifications for each DOG as well as the number of coauthors in agreement with the mode is useful as a qualititative assessment of the morphology for comparison with the more quantitative methods discussed below. Results are presented in Table 3 and discussed in section 4.2.1.

3.2.2. *Non-parametric Classification*

A wide variety of tools now exist to quantify the morphologies of galaxies. Five which frequently appear in the literature are the concentration index C (Abraham et al. 1994), the rotational asymmetry A (Schade et al. 1995), the residual clumpiness, S (Conselice 2003), the Gini coefficient G (Abraham et al. 2003), and M_{20} parameter (Lotz et al. 2004). Of these five, A and S have S/N and spatial resolution requirements that are not satisfied by the existing imaging of the DOGs in this sample (e.g., Lotz et al. 2004, show that significant type-dependent systematic offsets in A arise at per-pixel S/N< 5). Therefore, this analysis is focused on C, G, and M_{20}.

The concentration index C is defined as (Bershady et al. 2000):

$$C = 5\log 10 \left(\frac{r_{80}}{r_{20}} \right), \qquad (1)$$

where r_{80} and r_{20} are the radii of circular apertures containing 80% and 20% of the total flux, respectively. G was originally introduced to measure how evenly the wealth in a society is distributed (Glasser 1962). Recently, Abraham et al. (2003) and Lotz et al. (2004) applied this method to aid in galaxy classification: low values imply a galaxy's flux is well-distributed among many pixels, while high values imply a small fraction of the pixels within a galaxy account for the majority of the total flux. M_{20} is the logarithm of the second-order moment of the brightest 20% of the galaxy's flux, normalized by the total second-order moment (Lotz et al. 2004). Higher values of M_{20} indicate multiple bright clumps offset from the second-order moment center. Lower values are typical of centrally-dominated systems.

Prior to computing G or M_{20}, we first generate a catalog of objects using SExtractor (Bertin & Arnouts 1996). We use a detection threshold of 3σ (corresponding to 23.7 mag arcsec^{-2}) and a minimum detection area of 15 pixels. The number of deblending thresholds was 32, and the minimum contrast parameter for deblending was 0.1. We found by trial and error that these parameters minimized the separation of a single galaxy into multiple components.

For SST24 J143349.5+334602 and SST24 J142652.4+345504, examination of the F814W-F160W color indicated that a nearby neighbor with similar color

should not be excluded as a foreground/background object. For both DOGs, we modified the segmentation map to reflect this.

The final segmentation map produced by SExtractor (and modified in two cases) is used to mask out foreground/background objects (pixels that are masked out are simply not used in the remainder of the analysis). The center of the image, the ellipticity, and position angle computed by SExtractor are used as inputs to our morphology code. This code is written by J. Lotz and described in detail in Lotz et al. (2004). Here, we summarize the relevant information.

Postage stamps of each object in the SExtractor catalog (and the associated segmentation map) are created with foreground and background objects masked out. For each source, we adopt the sky value computed in our photometric analysis. Since the isophotal-based segmentation map produced by SExtractor is subject to the effects of surface brightness dimming at high redshift, pixels belonging to the galaxy are computed based on the surface brightness at the elliptical Petrosian radius, $\mu(r_P)$. We adopt the usual generalized definition for r_P as the radius at which the ratio of the surface brightness at r_P to the mean surface brightness within r_P is equal to 0.2 (Petrosian 1976). The elliptical r_P is derived from surface brightness measurements within elliptical apertures and represents the length of the major axis. Studies have shown that using the Petrosian radius to select pixels associated with a galaxy provides the most robust morphological measurements (Lotz et al. 2004; Lisker 2008). Pixels with surface brightness above $\mu(r_P)$ are assigned to the galaxy while those below it are not.

Using the new segmentation map, we recompute the galaxy's center by minimizing the total second-order moment of the flux. A new value of r_P is then computed and a revised segmentation map is used to calculate G and M_{20}. Finally, the morphology code calculates an average S/N per pixel value using the pixels in the revised segmentation map (Eqs. 1 through 5 in Lotz et al. 2004). The S/N per pixel and spatial resolution of each image is used to estimate the uncertainties in the morphological parameters of each galaxy. The uncertainties are derived from the rms variation between measurements of the same galaxies in GOODS images compared to UDF images (Lotz et al. 2006) and assumes that the UDF morphology measurements are "truth". Results of this analysis are presented in Table B1 and will be discussed in section 4.2.2.

3.2.3. *GALFIT Modeling*

In Paper I, we reported the existence of a centrally located, compact component that was present in the NICMOS images of power-law DOGs but absent in the ACS/WFPC2 images, signifying the presence of strong central obscuration. To quantify this feature, we used GALFIT (Peng et al. 2002) to model the 2-D light profile of the DOGs. In this paper, we repeat this procedure on the bump DOGs with *HST* NICMOS data. Here, we review our methodology.

We choose the size of the fitting region to be 41×41 pixels (corresponding to angular and physical sizes of 3″ and ≈24 kpc, respectively) because the DOGs are small and have low S/N compared to more typical applications of GALFIT. For the same reason, we wish to include

only the minimum necessary components in our model. We model the observed emission with three components which are described by a total of 10 free parameters. The number of degrees of freedom, $N_{\rm DOF}$, is calculated as the difference of the number of pixels in the image and the number of free parameters. Thus, the maximum $N_{\rm DOF}$ is 1671. Cases where $N_{\rm DOF} < 1671$ are associated with images where some pixels were masked out because they were associated with obvious residual instrumental noise. NIC2 is a Nyquist-sampled array ($0.075''$ pix^{-1} compared to $0.16''$ FWHM beam), so the pixels in our image are not completely independent and the χ_ν^2 values should be interpreted in a relative sense rather than an absolute one.

The first element in our GALFIT model is a sky component whose amplitude is held constant at a value derived from the photometry to yield flat radial profiles. The second is an instrumental PSF generated from the TinyTim software assuming a red power-law spectrum ($F_\nu \propto \nu^{-2}$) as the object spectrum (Krist and Hook 2004), which can simulate a PSF for NICMOS, WFPC2, and ACS. For the NICMOS and WFPC2 images, the DOG is positioned in nearly the same spot on the camera. In the case of WFPC2 this is pixel (132,144) of chip 3 and pixel (155, 164) for NICMOS. The PSF is computed out to a size of $3.0''$, and for the WFPC2 PSF we oversample by a factor of 1.3 to match the pixel scale of the drizzled WFPC2 images.

The final component is a Sérsic profile (Sersic 1968) where the surface brightness scales with radius as $\exp[-\kappa((r/R_{\rm eff})^{1/n} - 1)]$, where κ is chosen such that half of the flux falls within $R_{\rm eff}$. As few constraints as possible were placed so as to optimize the measurement of the extended flux (i.e., non-point source component). In certain cases, the Sérsic index had to be constrained to be positive to ensure convergence on a realistic solution. When fitting the NICMOS data, the uncertainty image from `calnicb` provides the necessary information required by GALFIT to perform a true χ^2 minimization. The TinyTim NIC2 PSF is convolved with the Sérsic profile prior to performing the χ^2 minimization. The initial guesses of the magnitude, half-light radius, position angle, and ellipticity were determined from the output values from SExtractor. Varying the initial guesses within reasonable values (e.g., plus or minus two pixels for the half-light radius) yielded no significant change in the best-fit model parameters. The NICMOS centroid was used as the initial guess for the (x,y) position of both the PSF and extended components.

A degeneracy potentially exists between our estimates of the point-source fraction (i.e., relative ratio of PSF component flux to Sérsic component flux) and the Sérsic index. Fits using models without the PSF component yield larger reduced χ_ν^2 values, especially when the point source fraction in our three-component model was large (see further discussion in section 4.2.3). In cases where the point source fraction was small, the no-PSF model had similar parameter values as our fiducial three-component model, as would be expected.

The results of this GALFIT analysis are presented in Table B1 and will be discussed in section 4.2.3.

It is important to note here that NIC2 cannot spatially resolve objects smaller than 1.3 kpc at $z \approx 2$. This limit
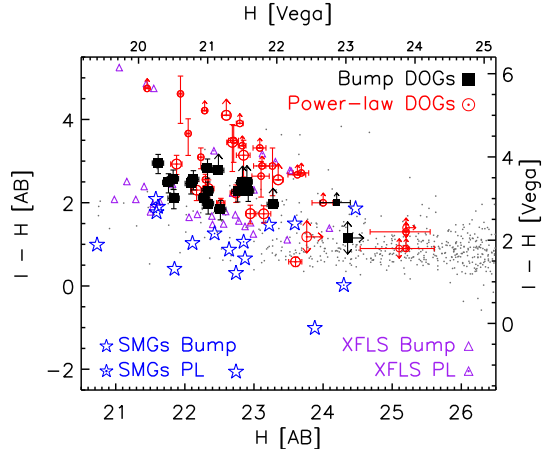

FIG. 3.— Color-magnitude diagram for bump DOGs, power-law DOGs , SMGs, and XFLS ULIRGs at $z > 1.4$ (symbols as in Figure 1). Smaller symbols indicate objects where the I-band measurement has been synthesized from the R-band or V-band measurement (Dasyra et al. 2008; Bussmann et al. 2009b), assuming a power-law of the form $F_\nu \propto \nu^{-2}$. Arrows indicate 2-σ limits. Galaxies spanning the redshift range $1.5 < z < 2.5$ in the HDF-N (Papovich, personal communication) and HDF-S (Labbé et al. 2003) are shown with grey dots. Power-law DOGs have the reddest $I - H$ colors, followed by bump DOGs, XFLS ULIRGs, and SMGs, which have colors comparable to high-z HDF galaxies.

is large enough to encompass a compact stellar bulge as well as an active galactic nucleus, implying that we cannot, from these data alone, distinguish between these two possibilities as to the nature of any central, unresolved component.

4. RESULTS

In this section, we present our photometry, visual classification, non-parametric classification, GALFIT modeling, and stellar and dust mass results.

4.1. *Photometry*

Table 2 presents the photometric information derived from the *HST* imaging. In Figure 3, we show the $I-H$ vs. H color-magnitude diagram for bump DOGs, power-law DOGs, XFLS ULIRGs, and a sample of galaxies in the Hubble Deep Field (HDF) whose photometric redshifts are comparable to DOGs ($1.5 < z_{\rm phot} < 2.5$). Power-law DOGs tend to be the reddest sources ($I - H \approx 2 - 5$ AB mag), followed by bump DOGs ($I - H \approx 2 - 3$ AB mag), XFLS ULIRGs ($I - H \approx 1.5 - 3$), and SMGs, which have $I - H$ colors similar to high-z galaxies in the HDF ($I - H \approx 0 - 2$ AB mag). SMGs and DOGs (both bump and power-law varieties) are comparably bright in H. The bluer color of SMGs relative to DOGs at a given H-band magnitude suggests weaker UV flux from DOGs, either due to older stellar populations in DOGs or a higher dust mass relative to stellar mass in DOGs.

4.2. *Morphologies*

4.2.1. *Visual Classification Results*

From the 7 users who entered classifications of the NICMOS images of DOGs, the main results can be summarized as follows: power-law DOGs were classified as irregular (43%) approximately as frequently as they were classified regular (42%), with 15% being too faint to tell. In contrast, bump DOGs were classified as irregular significantly more often than they were classified as regular

<div align="center">

TABLE 2
PHOTOMETRIC PROPERTIES

</div>

Source Name	$F_{\rm F814W}$ (μJy)	$\sigma_{\rm F814W}$ (μJy)	F_{F160W} (μJy)	σ_{F160W} (μJy)	F_{24} (mJy)	$R - [24]$ (Vega)
SST24 J142637.3+333025	0.36	0.19	0.45	0.57	0.64	>15.0
SST24 J142652.4+345504	0.24	0.15	1.78	0.36	1.29	15.0
SST24 J142724.9+350823	0.63	0.15	6.72	0.42	0.51	14.4
SST24 J142832.4+340850	0.59	0.16	—	—	0.52	13.9
SST24 J142920.1+333023	0.35	0.14	2.85	0.27	0.51	>13.6
SST24 J142941.0+340915	0.30	0.13	2.47	0.46	0.59	>14.6
SST24 J142951.1+342041	0.55	0.16	5.30	0.52	0.60	>14.9
SST24 J143020.4+330344	0.31	0.13	4.26	0.50	0.54	>15.3
SST24 J143028.5+343221	0.59	0.16	4.92	0.31	1.27	14.7
SST24 J143137.1+334500	0.18	0.14	2.67	0.37	0.57	14.3
SST24 J143143.3+324944	0.43	0.15	6.43	0.37	1.51	14.4
SST24 J143152.4+350029	0.54	0.16	8.21	0.31	0.52	14.3
SST24 J143216.8+335231	0.51	0.15	4.24	0.37	1.28	>16.1
SST24 J143321.8+342502	0.72	0.16	7.16	0.37	0.56	14.4
SST24 J143324.2+334239	0.96	0.17	6.67	0.47	0.53	13.8
SST24 J143331.9+352027	0.66	0.17	3.58	0.32	0.60	14.3
SST24 J143349.5+334602	0.63	0.15	4.44	0.33	0.53	14.3
SST24 J143458.8+333437	0.49	0.20	5.14	0.51	0.57	14.0
SST24 J143502.9+342657	0.24	0.13	2.52	0.63	0.50	14.1
SST24 J143503.3+340243	0.26	0.14	3.68	0.36	0.76	14.6
SST24 J143702.0+344631	0.10	0.11	0.17	0.33	0.33	14.2
SST24 J143816.6+333700	0.68	0.16	4.22	0.22	3.28	14.8

(69% vs. 26%, with only 5% being too faint to tell). These results can be subdivided into those with very robust classifications (6 or more users were in agreement), and less robust classifications (fewer than 6 users were in agreement). The trends quoted earlier become stronger when considering only the robust classifications, as the ratio of regular:irregular classifications for this subset is 1.4:1 and 1:3 for power-law and bump DOGs, respectively. Table 3 shows the breakdown of visual classifications with this additional subdivision. In Table B1 we provide, for each DOG in this sample, the mode of the classifications as well as how many users were in agreement with the mode. Overall, the qualitative morphological assessment indicates that bump DOGs have irregular, diffuse morphologies more frequently than power-law DOGs.

4.2.2. Non-parametric Classification Results

The characterization of galaxy morphologies requires high S/N imaging in order to provide reliable results. For non-parametric forms of analysis, typical requirements are $\rm S/N_{pixel} > 2$ and r_p(Elliptical) $> 2 \times$ FWHM (Lotz et al. 2004) (hereafter, $r_{\rm P}$ indicates the elliptical petrosian radius). In the case of the imaging presented here, FWHM $= 0\farcs16$. None of the 20 bump DOGs in this study observed with WFPC2 have the per-pixel S/N necessary to compute $r_{\rm P}$, G, M_{20}, and C. On the other hand, 18 out of 20 sources have sufficient S/N in the NICMOS imaging. Table B1 presents the visual and non-parametric measures of DOG morphologies, including per-pixel S/N, $r_{\rm P}$, G, M_{20}, and C values for the NICMOS images. This table also includes an estimate of whether the DOG is dominated by a bump or by a power-law in the mid-IR using IRAC data from Ashby et al. (2009) and the same statistical definition originally used by Dey et al. (2008).

Figure 4 displays C as a function of $r_{\rm P}$ for power-law DOGs, bump DOGs, SMGs, and XFLS sources. The error bars indicate the typical uncertainties in C and

$r_{\rm P}$ given the S/N and spatial resolution associated with the imaging of each galaxy. The left panel of Figure 4, focusing only on bump and power-law sources that qualify as DOGs, shows that bump DOGs have larger sizes (median $r_{\rm P} = 8.4$ kpc, $\sigma_{r_{\rm P}} = 2.7$ kpc) than their power-law counterparts (median $r_{\rm P} = 5.5$ kpc, $\sigma_{r_{\rm P}} = 2.3$ kpc). A two-sided Kolmogorov-Smirnov (KS) indicates only a 1% chance the two $r_{\rm P}$ distributions are drawn from the same parent distribution. The right panel of Figure 4 shows SMGs and XFLS sources which are not DOGs. In this diagram, almost all sources are bumps, and almost all sources have large sizes (median $r_{\rm P} = 8.5$ kpc, $\sigma_{r_{\rm P}} = 2.9$ kpc).

When no consideration is given to their $R - [24]$ color, SMGs and XFLS sources show a similar distinction in their sizes when dividing the samples into bump (SMG median $r_{\rm P} = 8.6$ kpc, $\sigma_{r_{\rm P}} = 3.3$ kpc; XFLS median $r_{\rm P} = 7.6$ kpc, $\sigma_{r_{\rm P}} = 2.9$ kpc) and power-law (SMG median $r_{\rm P} = 4.6$ kpc, $\sigma_{r_{\rm P}} = 4.5$ kpc; XFLS median $r_{\rm P} = 4.8$ kpc, $\sigma_{r_{\rm P}} = 1.5$ kpc) varieties. Indeed, considering all $z > 1.4$ ULIRGs regardless of whether they are selected at mid-IR or sub-mm wavelengths, bump sources (median $r_{\rm P} = 8.4$ kpc, $\sigma_{r_{\rm P}} = 2.9$ kpc) are significantly larger than their power-law counterparts (median $r_{\rm P} = 5.6$ kpc, $\sigma_{r_{\rm P}} = 1.9$ kpc), and a two-sided KS test indicates there is only a 1.3% chance the two populations could be drawn randomly from the same parent sample. This finding is consistent with results from Keck K-band adaptive optics imaging of DOGs which shows that power-law DOGs are smaller and more concentrated than bump DOGs (Melbourne et al. 2009). One caveat with this result is that the bump DOG sample is brighter in H-band than the power-law DOG sample. Considering only the DOGs satisfying $H < 22.5$, the bump and power-law DOGs have similar sizes ($r_{\rm P} \approx 8$ kpc). At the faint end ($H > 22.5$), power-law DOGs are smaller than bump DOGs (5 kpc vs. 8 kpc, respectively).

The distribution in $G - M_{20}$ space derived from NICMOS imaging of power-law DOGs, bump DOGs, XFLS

TABLE 3
VISUAL MORPHOLOGICAL CLASSIFICATIONS

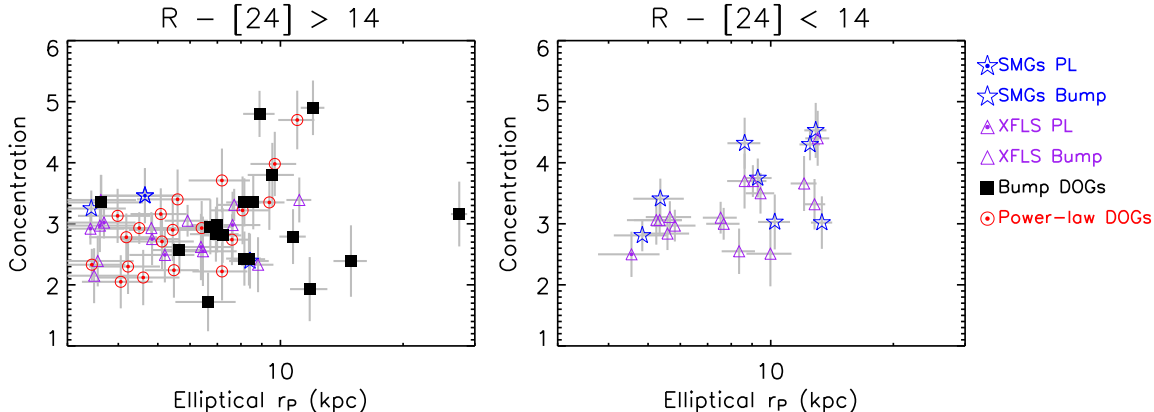|	Regular		Irregular		Too Faint	Too Tell
	Agree	Disagree	Agree	Disagree	Agree	Disagree
Power-law DOGs	34%	9%	24%	18%	6%	9%
Bump DOGs	16%	10%	48%	21%	5%	0%

FIG. 4.— C as a function of r_P for $z > 1.4$ ULIRGs (symbols are the same as in Figure 1). *Left*: Power-law DOGs, bump DOGs, SMGs that qualify as DOGs, and XFLS ULIRGs at $z > 1.4$ that qualify as DOGs. Error bars illustrate the typical uncertainty level given the S/N and spatial resolution associated with the image of each galaxy (Lotz et al. 2006). Bump DOGs have larger sizes than power-law DOGs. *Right*: Same as left panel, but only for $z > 1.4$ ULIRGs (SMGs and XFLS) that are not DOGs. Regardless of sample selection criteria, power-law $z > 1.4$ ULIRGs are significantly smaller than their bump counterparts (median r_P of 5.6 kpc vs. 8.0 kpc, for the total respective populations).

sources, and SMGs is shown in Figure 5. The error bars indicate the typical uncertainties in G and M_{20} given the S/N and spatial resolution of the imaging of each galaxy. A sample of 73 local ULIRGs ($z < 0.2$) is also shown in this diagram (Lotz et al. 2004), using data from *HST* WFPC2/F814W imaging (Borne et al. 2000). The dotted line separates major mergers from other types of galaxies and is based on measurements at roughly the same rest-frame wavelength ($\approx 5000 - 5500$ Å) of these 73 local ULIRGs (Lotz et al. 2004).

The left panel of Figure 5 (including all sources that qualify as DOGs) shows that bump DOGs appear offset to lower G and higher M_{20} values than power-law DOGs. The median $\{G, M_{20}\}$ values for bump and power-law DOGs are $\{0.47, -1.08\}$ and $\{0.49, -1.48\}$, respectively. A two-sided KS test indicates that there is only a 0.5% chance that the two M_{20} distributions could have been drawn randomly from the same parent distribution (the two G distributions have a 10% chance of being drawn from the same parent distribution). These types of morphologies are consistent with what is seen in simulations of major mergers during the beginning and end stages, respectively, of the "final coalescence" of the merger when the SFR peaks and begins to turn over (Lotz et al. 2008). In the right panel of Figure 5, SMGs and XFLS $z > 1.4$ ULIRGs that are not DOGs are shown. Although nearly all of these sources have bump SEDs, their morphologies bear a greater resemblence to power-law DOGs than bump DOGs. The median $\{G, M_{20}\}$ values for the non-DOGs are $\{0.52, -1.46\}$.

The preceding analysis is largely qualitative in nature. A more quantitative approach involves the use of contingency tables, which offer a means to quantify broad-brush distinctions in the properties of two populations

of objects. Three properties are tested here: mid-IR SED shape (bump OR power-law), extent of obscuration ($R - [24] > 14$ OR $R - [24] < 14$), and morphology (low G, high M_{20} OR high G, low M_{20}). The division based on morphology is derived from simulations of major mergers, which indicate that the high SFR period of a merger is bisected by a line described by the equation $G = 0.4 M_{20} + 0.9$ (Lotz et al. 2008). Table 4 shows the two 2×2 contingency tables that are needed to account for the three variables used in this analysis.

The first result from this analysis is the paucity of power-law sources in the non-DOG subset. There are 29 bump DOGs, 23 bump non-DOGs, 31 power-law DOGs, and only 1 power-law non-DOGs. The 2×2 contingency table for this dataset indicates a negligible probability (Fisher Exact p-value < 0.0001) that all four sub-populations are drawn randomly from the same parent sample. Could this be due to a selection effect? The non-DOG sample comprises ULIRGs from the XFLS and SMGs. XFLS sources are selected to have high $F_{24\mu m}/F_{8\mu m}$ flux density ratios, which tends to favor the selection of bump SEDs over power-law ones. On the other hand, the XFLS sources are selected to be very bright at $24\mu m$ ($F_{24\mu m} > 0.8$ mJy. At these $24\mu m$ flux densities, power-law sources are more common than bump sources (e.g. Dey et al. 2008). SMGs are selected at sub-mm wavlengths, without any knowledge of the mid-IR SED shape. Presently, it is not obvious that either the XFLS ULIRGs or SMGs are affected by the kind of severe selection effect necessary to produce the observed trends.

The second result from the contingency table data is that, considering only bump sources, non-DOGs have a much more skewed distribution of morphologies than
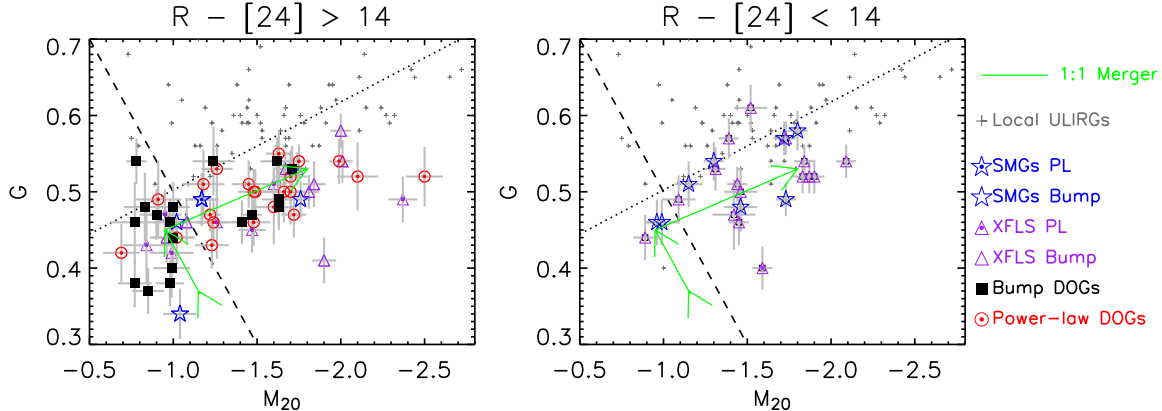
FIG. 5.— Gini coefficient vs. M_{20} derived from NIC2/F160W images of high-redshift ULIRGs (symbols same as in Figure 4) and local ULIRGs (gray plus signs, Lotz et al. 2004). The evolution of a typical gas-rich ($f_{gas} = 0.5$) major merger during its peak SFR period is illustrated by a green vector (Lotz et al. 2008). The dashed line is drawn qualitatively to separate "diffuse" and "single-object" morphologies and bisects the green vector. The dotted line shows the empirically determined (based on measurements of local ULIRGs) demarcation line above which objects are obvious major mergers (Lotz et al. 2004). *Left*: Bump DOGs, power-law DOGs, and SMGs and XFLS ULIRGs qualifying as DOGs. Within this highly obscured subset of the high redshift ULIRG population, bump sources are "diffuse" (low G, high M_{20}) more often than power-law DOGs. In simulations of major mergers, such morphologies occur during the early half of the peak SFR period of the merger. *Right*: Same as left panel, but for SMGs and XFLS $z > 1.4$ ULIRGs that are not DOGs. The distribution of morphologies for non-DOGs is skewed towards the "single-object" region of this diagram. These objects may occur during the late stage of the peak SFR period of a major merger, or they may be associated with more secular evolutionary processes.

TABLE 4
NICMOS MORPHOLOGY CONTINGENCY TABLE DATA

| | $R - [24] < 14$ | | $R - [24] > 14$ | |
	Diffuse[a]	Single-source[b]	Diffuse[a]	Single-source[b]
Power-law	0	1	7	24
Bump	3	20	15	14

[a] $G < 0.4 M_{20} + 0.9$
[b] $G > 0.4 M_{20} + 0.9$

DOGs. Diffuse type morphologies (low G, high M_{20}) are rare in the non-DOG population, while in DOGs they occur much more frequently. A 2×2 contingency table here suggests a very low probability (Fisher Exact p-value = 0.007) that blue ($R-[24] < 14$) and red ($R-[24] > 14$) ULIRGs have morphologies drawn from the same parent distribution. Low G and high M_{20} values suggest irregular and lumpy (less centrally concentrated) morphologies that could be caused by a clumpy distribution of stars or significant dust obscuration (Lotz et al. 2008). Further discussion of the implications of this result are deferred to section 5.

Finally, with the highly obscured subset of ULIRGs (DOGs), there is evidence that bump DOGs have diffuse type morphologies more commonly than power-law DOGs. A 2×2 contingency table indicates an extremely low probability (Fisher Exact p-value = 0.003) that bump and power-law DOGs have morphologies drawn from the same parent distribution. As mentioned earlier, this distinction is consistent with expectations from simulations of major mergers during the peak SFR phase of the merger (Lotz et al. 2008).

4.2.3. *GALFIT Results*

The results of our GALFIT analysis of the NICMOS images of the Cycle 16 DOGs are shown in Table B1, along with 1-σ uncertainties in the best-fit parameters. Included in this table are point source fractions (ratio of flux in the point-source component to the total flux of the

source), effective radius of the Sérsic component (R_{eff}), Sérsic index (n), semi-minor to semi-major axis ratio of the Sérsic component (Axial Ratio), number of degrees of freedom (N_{DOF}), and reduced chi-squared (χ^2_ν).

Figure 6 shows a comparison of R_{eff} (the radius within which half the light is enclosed) and r_P (the radius at which the ratio of the surface brightness at r_P to the mean surface brightness within r_P is equal to 0.2) for DOGs, SMGs, and XFLS ULIRGs at $z > 1.4$. For bump DOGs and power-law DOGs, the median R_{eff} values are 3.3 kpc and 2.5 kpc, respectively. Bump sources that are not DOGs (from the SMG and XFLS samples) have a median effective radius of 3.2 kpc. One of the bump DOGs (SST24 J143137.1+334500) has the appearance of an edge-on disk with a semi-major axis of $3''25$, or 27.5 kpc at its redshift of 1.77. This extremely large R_{eff} value may imply that this object is in fact a merger viewed edge-on. Spatially resolved dynamical information would be particularly useful for answering this question.

Our measurements of SMG sizes (median R_{reff} value for the full SMG population of 3.6 kpc) are in broad agreement, given the different methods used, with those of Swinbank et al. (2010), who find typical half-light radii of 2.8 ± 0.4 kpc. For XFLS ULIRGs, Dasyra et al. (2008) use GALFIT to find typical effective radii of 2.43 ± 0.80 kpc, consistent with our results (median R_{eff} of 2.5 kpc). As an additional consistency check, a strong correlation is evident between R_{eff} and r_P for all populations. Note that $r_P > R_{eff}$; this is because the Sérsic profile is defined such that half of the galaxy's flux is enclosed within a radius of $r = R_{eff}$, while r_P defines the radius at which the surface brightness is one-fifth the average surface brightness within r_P.

Figure 7 shows the point source fraction and Sérsic index for DOGs, SMGs, and XFLS ULIRGs at $z > 1.4$. The majority of sources have low point source fractions (point source fraction < 0.3) and disk-type morphologies ($n < 2$). Studies have found that when a point source contributes less than 20% of the total light, it has an in-
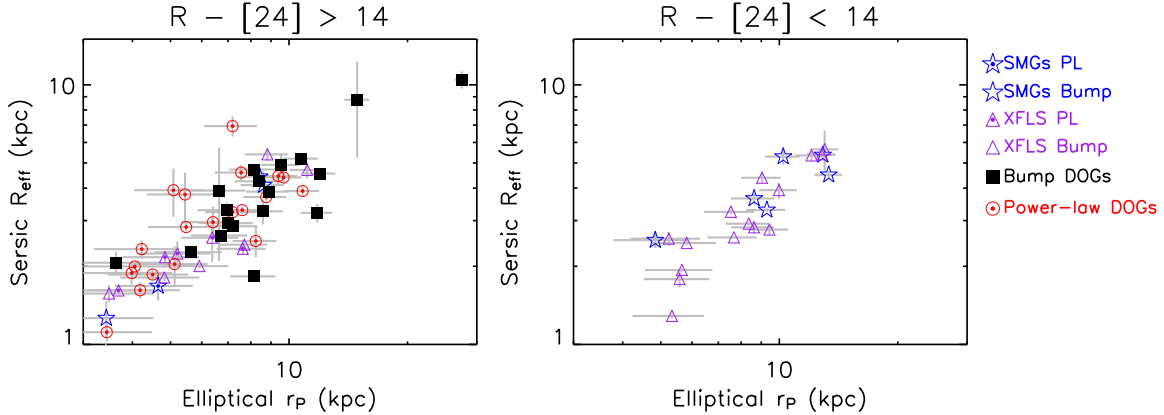
FIG. 6.— Comparison of sizes of $z > 1.4$ ULIRGs (symbols same as in Figure 4) as determined by the effective radius of the Sérsic component from GALFIT modeling ($R_{\rm eff}$) and the elliptical Petrosian radius ($r_{\rm P}$). Error bars represent 1σ uncertainty values from GALFIT. *Left*: Bump DOGs, power-law DOGs, and SMGs and XFLS ULIRGs qualifying as DOGs. *Right*: SMGs and XFLS ULIRGs that are not DOGs. Both size measurements suggest that power-law sources are on average smaller than bump sources, although a significant population of compact bump sources exists.

significant effect on the measured morphologies (Pierce et al. 2010). Considering only DOGs with sufficient S/N to be placed on this diagram (left panel of Figure 7), 6/28 power-law DOGs and 0/17 bump DOGs have either $n > 3$ or point source fraction > 0.4. Such sources have compact, centrally dominated morphologies ($n = 1$ corresponds to an exponential profile, and $n = 4$ corresponds to a de Vaucouleurs profile; Peng et al. 2002). This distinction is consistent with the G and M_{20} results in section 4.2.2.

On the other hand, the distinction between bump and power-law sources is not as obvious when considering the SMGs and XFLS sources. For SMGs, 2/3 power-law and 2/11 bump sources satisfy the compact criteria outlined above, while for XFLS ULIRGs the respective numbers are 2/6 (power-law sources) and 3/18 (bump sources). Further discussion of the distinction between the morphological properties of bump and power-law DOGs is deferred to section 5.

5. DISCUSSION: IMPLICATIONS FOR MODELS OF MASSIVE GALAXY EVOLUTION

ULIRG activity in the local universe has been known for some time to result from a major merger of two gas-rich disk galaxies (e.g. Armus et al. 1987; Sanders et al. 1988a). Material is funneled towards the center of the system and drives an intense starburst, producing large amounts of cold dust, and begins to feed a nascent central black hole. As the merger evolves, ambient gas and dust particles are heated by feedback processes. This warm-dust ULIRG stage has been suggested to represent a transition stage between cold ULIRGs and optically luminous quasars (Sanders et al. 1988b).

Recently, efforts have been made to extend this paradigm to the ultra-luminous galaxy populations at high-redshift. One possible hypothesis within this scenario is that SMGs represent the cold-dust ULIRGs created during the early stage of the merger, whereas *Spitzer*-selected sources represent the warm-dust ULIRGs formed during the later stages of the merger (e.g., Dey et al. 2008; Dey & The NDWFS/MIPS Collaboration 2009; Narayanan et al. 2009). This basic picture (that SMGs and *Spitzer*-selected ULIRGs are related) is strengthened by the similarity in the measured clustering strengths of $z \approx 2$ SMGs, DOGs, and QSOs, which

suggest that these populations all reside in similar mass halos at similar epochs (e.g., Brodwin et al. 2008; Dey & The NDWFS/MIPS Collaboration 2009).

In this section, we test the viability of this scenario using the morphological evidence presented in section 4. On one hand, when considering only the most extremely obscured objects (i.e., DOGs), a clear trend in morphologies emerges. Bump DOGs are larger (i.e., more spatially extended) than power-law DOGs ($r_{\rm P} \approx 8$ kpc vs. 5 kpc), more diffuse ($\{G, M_{20}\} \approx \{0.47, -1.08\}$ vs. $\{G, M_{20}\} \approx \{0.49, -1.48\}$), and more irregular (67% vs. 50% visually classified as irregular). This trend is consistent with expectations from simulations of major mergers, which indicate that merger morphologies generally evolve from extended, diffuse, and irregular at the beginning of the peak SFR phase to compact and regular when star-formation shuts down and the AGN begins to dominate (Lotz et al. 2008; Narayanan et al. 2009).

On the other hand, the less obscured sources (non-DOGs from the SMG and XFLS sample) show two strong distinctions from their more extreme counterparts. First, there are very few power-law non-DOGs. If power-law SEDs are more frequently associated with objects that are more dust reddened, this may imply a connection between the amount of extinction of the optical light and the nature of the power source producing the mid-IR emission.

Second, within the bump population of non-DOGs, there are very few diffuse type morphologies (low G, high M_{20}). The prevalence of bump sources with "single-object" morphologies is difficult to understand within the context of a major merger scenario in which bump sources evolve into power-law sources. If the bump phase always precedes the power-law phase, there should be very few bump sources with compact, single-object morphologies. A number of potential explanations exist.

Perhaps the most exciting explanation is that high redshift ULIRGs are related to one another within a single evolutionary scheme driven by major mergers, but with an additional wrinkle related to the degree of obscuration. During the highly dust-obscured period of the merger (represented jointly by both bump and power-law DOGs), the bump phase typically occurs before the power-law phase. In contrast, the less obscured sources
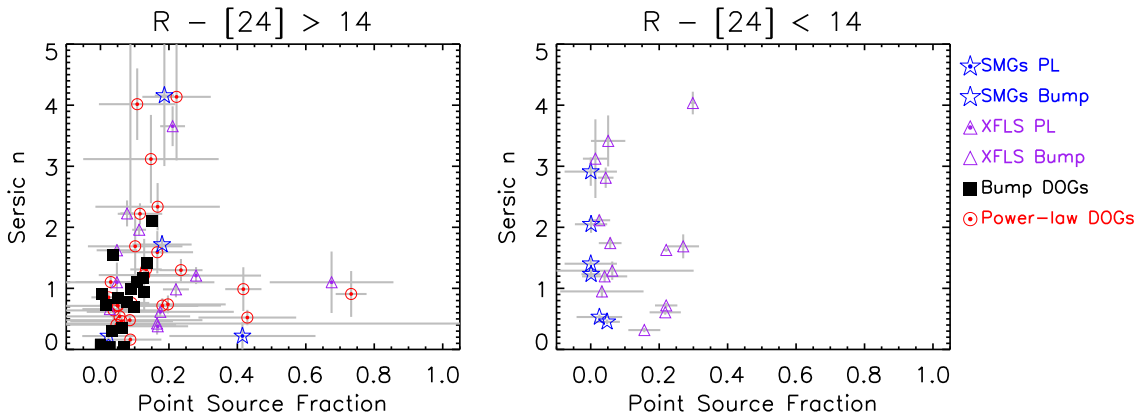
FIG. 7.— Sérsic index n as a function of point source fraction from GALFIT modeling (symbols same as in Figure 6). *Left*: Power-law DOGs, bump DOGs, and SMGs and XFLS ULIRGs qualifying as DOGs. Aside from a handful of power-law DOGs with point source fraction > 0.4 or $n > 2.5$, there is strong overlap between the bump and power-law DOG populations in this diagram. *Right*: SMGs and XFLS ULIRGs that do not qualify as DOGs. In contrast to the DOG populations, there are a number of $n > 2.5$ bump sources from the SMG and XFLS samples. As in the analysis of the G and M_{20} values, these could represent objects at the end of the peak SFR period, or they might not be associated with major merger activity at all.

(SMGs and XFLS ULIRGs) sample the merger over a broader timescale and so the relationship between bump and power-law sources is not as obvious. For example, there may be a significant population of blue ULIRGs (non-DOGs) that correspond to the systems near the very end of the high SFR period of the merger when the obscuring column of dust has decreased and UV light can escape the galaxy.

An alternative, but potentially equally exciting, way to reconcile the morphological evidence is by appealing to more quiescent modes of galaxy assembly for some fraction of the high redshift ULIRG population (e.g. Genzel et al. 2008). Recent theoretical work has suggested that many SMGs may be produced not by major mergers, but instead by smooth gas inflow and the accretion of small gas-rich satellites (?). Such an explanation would be surprising, given the evidence already in place favoring a major merger origin for SMGs largely based on dynamical and kinematic arguments (e.g. Greve et al. 2005; Swinbank et al. 2006; Tacconi et al. 2008; Engel et al. 2010). While there is no definitive evidence in the data presented here that can unambiguously support this smooth inflow mode of galaxy formation, the relatively normal morphologies observed in the non-DOGs could suggest that major mergers are not responsible for driving the prodigious on-going star-formation in these systems. Given that such intense star-formation bursts can only be sustained over a short timescale, the morphologies suggest that the fuel may have to be accreted in less disruptive minor mergers or through some smooth process. Physical mechanisms explaining how such a process might occur have been presented recently (Genel et al. 2010,?). Observations of the internal dynamics of these systems (along the lines of, e.g., Genzel et al. 2008; Förster Schreiber et al. 2010; Genzel et al. 2010) are likely what is needed to continue progress in this area of research.

A third possibility is that the expected trends in morphologies with merger stage are somewhat sensitive both to the initial conditions of the merger — for example, highly radial orbits can have similar G and M_{20} values throughout the "final merger" stage (Lotz et al. 2008) — as well as the viewing time and angle. It would be surprising if unusual initial conditions or viewing times and angles were necessary to explain most high redshift ULIRGs, particularly since they appear to have fairly typical axial ratios (see Table B1).

An important consideration related to the XFLS ULIRGs and SMGs analyzed here is that many of these objects are composite starburst and AGN systems with complex mid-IR spectral features. Dasyra et al. (2008) show that the 7.7μm PAH feature is usually strong in extended sources, while it varies from strong to weak in compact sources. The mid-IR spectral analysis of these sources (Sajina et al. 2007) indicates that only a few XFLS ULIRGs are clearly dominated by PAH features or AGN continuum emission. This result is consistent with the nature of their mid-IR SEDs and underscores the fact that these objects are composite systems that are not easily classified by either their mid-IR spectral features or their rest-frame optical morphologies. Only 7 SMGs in the sample studied here have both high-resolution imaging and mid-IR spectroscopy (Menéndez-Delmestre et al. 2009). Of these 7, all are bump sources, 4 have strong PAH emission, and 3 have weak or no PAH emission. It may be the case that the mid-IR SEDs of the SMG and XFLS ULIRG samples are not sufficiently distinct to identify significant morphology differences in the bump vs. power-law sub-samples.

6. CONCLUSIONS

We have used *HST* imaging to analyze the morphologies of 22 DOGs at $z \approx 2$ from the Boötes field selected to show SED features typical of star-formation dominated systems (bump DOGs). We compare these new data with similar *HST* imaging of DOGs with SED features typical of AGN-dominated systems (power-law DOGs), submillimeter galaxies (SMGs), and a sample of ULIRGs at high-z selected from the *Spitzer* XFLS. Our findings are summarized below.

1. Spatially resolved emission is observed in the rest-frame optical imaging of all bump DOGs. GALFIT modeling indicates that the point source fraction (ratio of flux in the point-source component to total flux of the source) in these objects never exceeds 20% and is typically smaller than that found in

power-law DOGs, suggesting a smaller AGN contribution to the rest-frame optical light from bump DOGs.

2. Typical Sérsic indices of the resolved emission of bump DOGs suggest disk-type rather than bulge-type profiles ($n < 2$), similar to power-law DOGs.

3. At $H < 22.5$, bump and power-law DOGs have similar sizes (median $r_P = 8$ kpc). At $H > 22.5$, bump DOGs are significantly larger than power-law DOGs (median value of $r_P = 8$ kpc vs. $r_P = 5.4$ kpc, respectively). This distinction is also true for SMGs and XFLS ULIRGs.

4. In the rest-frame optical, bump DOGs have lower G and higher M_{20} values than power-law DOGs. This difference is consistent with expectations from simulations of major mergers. On the other hand, less obscured objects in our sample (SMGs and XFLS ULIRGs that do not qualify as DOGs) have high G and low M_{20} values that are more typical of "single-object" systems.

Overall, our findings highlight the diversity and complexity of high redshift ULIRG morphologies. Within the highly obscured subset (i.e., DOGs), we find evidence in support of a major merger paradigm in which bump DOGs evolve into power-law DOGs. Within the less obscured subset (i.e., SMGs and XFLS ULIRGs), the picture is not as clear. This may be a result of the timescales over which obscured and less obscured sources can be observed during a major merger. Alternatively, that the intense star-formation in these less-obscured ULIRGs is not the result of a recent major merger, and may be an indication that more quiescent forms of galaxy assembly are important for some high redshift ULIRGs.

REFERENCES

Abraham, R. G., Valdes, F., Yee, H. K. C., & van den Bergh, S. 1994, ApJ, 432, 75
Abraham, R. G., van den Bergh, S., & Nair, P. 2003, ApJ, 588, 218
Armus, L., Heckman, T., & Miley, G. 1987, AJ, 94, 831
Ashby, M. L. N., Stern, D., Brodwin, M., Griffith, R., Eisenhardt, P., Kozłowski, S., Kochanek, C. S., Bock, J. J., Borys, C., Brand, K., Brown, M. J. I., Cool, R., Cooray, A., Croft, S., Dey, A., Eisenstein, D., Gonzalez, A. H., Gorjian, V., Grogin, N. A., Ivison, R. J., Jacob, J., Jannuzi, B. T., Mainzer, A., Moustakas, L. A., Röttgering, H. J. A., Seymour, N., Smith, H. A., Stanford, S. A., Stauffer, J. R., Sullivan, I., van Breugel, W., Willner, S. P., & Wright, E. L. 2009, ApJ, 701, 428
Bershady, M. A., Jangren, A., & Conselice, C. J. 2000, AJ, 119, 2645
Bertin, E. & Arnouts, S. 1996, A&AS, 117, 393
Blain, A. W., Chapman, S. C., Smail, I., & Ivison, R. 2004, ApJ, 611, 725
Borne, K. D., Bushouse, H., Lucas, R. A., & Colina, L. 2000, ApJ, 529, L77
Brand, K., Dey, A., Desai, V., Soifer, B. T., Bian, C., Armus, L., Brown, M. J. I., Le Floc'h, E., Higdon, S. J., Houck, J. R., Jannuzi, B. T., & Weedman, D. W. 2007, ApJ, 663, 204
Brand, K., Weedman, D. W., Desai, V., Le Floc'h, E., Armus, L., Dey, A., Houck, J. R., Jannuzi, B. T., Smith, H. A., & Soifer, B. T. 2008, ApJ, 680, 119
Brodwin, M., Dey, A., Brown, M. J. I., Pope, A., Armus, L., Bussmann, S., Desai, V., Jannuzi, B. T., & Le Floc'h, E. 2008, ApJ, 687, L65
Bussmann, R. S., Dey, A., Borys, C., Desai, V., Jannuzi, B. T., Le Floc'h, E., Melbourne, J., Sheth, K., & Soifer, B. T. 2009a, ApJ, 705, 184

Bussmann, R. S., Dey, A., Lotz, J., Armus, L., Brand, K., Brown, M. J. I., Desai, V., Eisenhardt, P., Higdon, J., Higdon, S., Jannuzi, B. T., LeFloc'h, E., Melbourne, J., Soifer, B. T., & Weedman, D. 2009b, ApJ, 693, 750
Chapman, S. C., Blain, A. W., Smail, I., & Ivison, R. J. 2005, ApJ, 622, 772
Conselice, C. J. 2003, ApJS, 147, 1
Coppin, K., Chapin, E. L., Mortier, A. M. J., Scott, S. E., Borys, C., Dunlop, J. S., Halpern, M., Hughes, D. H., Pope, A., Scott, D., Serjeant, S., Wagg, J., Alexander, D. M., Almaini, O., Aretxaga, I., Babbedge, T., Best, P. N., Blain, A., Chapman, S., Clements, D. L., Crawford, M., Dunne, L., Eales, S. A., Edge, A. C., Farrah, D., Gaztañaga, E., Gear, W. K., Granato, G. L., Greve, T. R., Fox, M., Ivison, R. J., Jarvis, M. J., Jenness, T., Lacey, C., Lepage, K., Mann, R. G., Marsden, G., Martinez-Sansigre, A., Oliver, S., Page, M. J., Peacock, J. A., Pearson, C. P., Percival, W. J., Priddey, R. S., Rawlings, S., Rowan-Robinson, M., Savage, R. S., Seigar, M., Sekiguchi, K., Silva, L., Simpson, C., Smail, I., Stevens, J. A., Takagi, T., Vaccari, M., van Kampen, E., & Willott, C. J. 2006, MNRAS, 372, 1621
Coppin, K., Halpern, M., Scott, D., Borys, C., Dunlop, J., Dunne, L., Ivison, R., Wagg, J., Aretxaga, I., Battistelli, E., Benson, A., Blain, A., Chapman, S., Clements, D., Dye, S., Farrah, D., Hughes, D., Jenness, T., van Kampen, E., Lacey, C., Mortier, A., Pope, A., Priddey, R., Serjeant, S., Smail, I., Stevens, J., & Vaccari, M. 2008, MNRAS, 384, 1597
Dasyra, K. M., Yan, L., Helou, G., Surace, J., Sajina, A., & Colbert, J. 2008, ApJ, 680, 232
Davé, R., Finlator, K., Oppenheimer, B. D., Fardal, M., Katz, N., Kereš, D., & Weinberg, D. H. 2010, MNRAS, 404, 1355

Desai, V., Soifer, B. T., Dey, A., Le Floc'h, E., Armus, L., Brand, K., Brown, M. J. I., Brodwin, M., Jannuzi, B. T., Houck, J. R., Weedman, D. W., Ashby, M. L. N., Gonzalez, A., Huang, J., Smith, H. A., Teplitz, H., Willner, S. P., & Melbourne, J. 2009, ApJ, 700, 1190

Dey, A., Soifer, B. T., Desai, V., Brand, K., Le Floc'h, E., Brown, M. J. I., Jannuzi, B. T., Armus, L., Bussmann, S., Brodwin, M., Bian, C., Eisenhardt, P., Higdon, S. J., Weedman, D., & Willner, S. P. 2008, ApJ, 677, 943

Dey, A. & The NDWFS/MIPS Collaboration. 2009, in Astronomical Society of the Pacific Conference Series, Vol. 408, Astronomical Society of the Pacific Conference Series, ed. W. Wang, Z. Yang, Z. Luo, & Z. Chen, 411–+

Donley, J. L., Rieke, G. H., Pérez-González, P. G., Rigby, J. R., & Alonso-Herrero, A. 2007, ApJ, 660, 167

Eisenhardt, P. R., Stern, D., Brodwin, M., Fazio, G. G., Rieke, G. H., Rieke, M. J., Werner, M. W., Wright, E. L., Allen, L. E., Arendt, R. G., Ashby, M. L. N., Barmby, P., Forrest, W. J., Hora, J. L., Huang, J.-S., Huchra, J., Pahre, M. A., Pipher, J. L., Reach, W. T., Smith, H. A., Stauffer, J. R., Wang, Z., Willner, S. P., Brown, M. J. I., Dey, A., Jannuzi, B. T., & Tiede, G. P. 2004, ApJS, 154, 48

Engel, H., et al. 2010, ApJ, 724, 233

Farrah, D., Lonsdale, C. J., Borys, C., Fang, F., Waddington, I., Oliver, S., Rowan-Robinson, M., Babbedge, T., Shupe, D., Polletta, M., Smith, H. E., & Surace, J. 2006, ApJ, 641, L17

Fiolet, N., Omont, A., Polletta, M., Owen, F., Berta, S., Shupe, D., Siana, B., Lonsdale, C., Strazzullo, V., Pannella, M., Baker, A. J., Beelen, A., Biggs, A., De Breuck, C., Farrah, D., Ivison, R., Lagache, G., Lutz, D., Tacconi, L. J., & Zylka, R. 2009, A&A, 508, 117

Fiore, F., Grazian, A., Santini, P., Puccetti, S., Brusa, M., Feruglio, C., Fontana, A., Giallongo, E., Comastri, A., Gruppioni, C., Pozzi, F., Zamorani, G., & Vignali, C. 2008, ApJ, 672, 94

Förster Schreiber, N. M., Shapley, A. E., Erb, D. K., Genzel, R., Steidel, C. C., Bouché, N., Cresci, G., & Davies, R. 2010, arXiv:1011.1507

Genel, S., Bouché, N., Naab, T., Sternberg, A., & Genzel, R. 2010, ApJ, 719, 229

Genel, S., et al. 2010, arXiv:1011.0433

Genzel, R., Burkert, A., Bouché, N., Cresci, G., Förster Schreiber, N. M., Shapley, A., Shapiro, K., Tacconi, L. J., Buschkamp, P., Cimatti, A., Daddi, E., Davies, R., Eisenhauer, F., Erb, D. K., Genel, S., Gerhard, O., Hicks, E., Lutz, D., Naab, T., Ott, T., Rabien, S., Renzini, A., Steidel, C. C., Sternberg, A., & Lilly, S. J. 2008, ApJ, 687, 59

Genzel, R., et al. 2010, arXiv:1011.536

Glasser, G. J. 1962, Journal of the American Statistical Association, 57, 648

Greve, T. R., Bertoldi, F., Smail, I., Neri, R., Chapman, S. C., Blain, A. W., Ivison, R. J., Genzel, R., Omont, A., Cox, P., Tacconi, L., & Kneib, J.-P. 2005, MNRAS, 359, 1165

Hainline, L. J., Blain, A. W., Smail, I., Frayer, D. T., Chapman, S. C., Ivison, R. J., & Alexander, D. M. 2009, ApJ, 699, 1610

Hopkins, P. F., Hernquist, L., Cox, T. J., Di Matteo, T., Robertson, B., & Springel, V. 2006, ApJS, 163, 1

Houck, J. R., Soifer, B. T., Weedman, D., Higdon, S. J. U., Higdon, J. L., Herter, T., Brown, M. J. I., Dey, A., Jannuzi, B. T., Le Floc'h, E., Rieke, M., Armus, L., Charmandaris, V., Brandl, B. R., & Teplitz, H. I. 2005, ApJ, 622, L105

Huang, J., Faber, S. M., Daddi, E., Laird, E. S., Lai, K., Omont, A., Wu, Y., Younger, J. D., Bundy, K., Cattaneo, A., Chapman, S. C., Conselice, C. J., Dickinson, M., Egami, E., Fazio, G. G., Im, M., Koo, D., Le Floc'h, E., Papovich, C., Rigopoulou, D., Smail, I., Song, M., Van de Werf, P. P., Webb, T. M. A., Willmer, C. N. A., Willner, S. P., & Yan, L. 2009, ApJ, 700, 183

Jannuzi, B. T. & Dey, A. 1999, in Astronomical Society of the Pacific Conference Series, Vol. 191, Photometric Redshifts and the Detection of High Redshift Galaxies, ed. R. Weymann, L. Storrie-Lombardi, M. Sawicki, & R. Brunner, 111–+

Koekemoer, A. M., Fruchter, A. S., Hook, R. N., & Hack, W. 2002, in The 2002 HST Calibration Workshop : Hubble after the Installation of the ACS and the NICMOS Cooling System, Proceedings of a Workshop held at the Space Telescope Science Institute, Baltimore, Maryland, October 17 and 18, 2002. Edited by Santiago Arribas, Anton Koekemoer, and Brad Whitmore. Baltimore, MD: Space Telescope Science Institute, 2002., p.337, ed. S. Arribas, A. Koekemoer, & B. Whitmore, 337–+

Kovács, A., Chapman, S. C., Dowell, C. D., Blain, A. W., Ivison, R. J., Smail, I., & Phillips, T. G. 2006, ApJ, 650, 592

Labbé, I., Franx, M., Rudnick, G., Schreiber, N. M. F., Rix, H.-W., Moorwood, A., van Dokkum, P. G., van der Werf, P., Röttgering, H., van Starkenburg, L., van de Wel, A., Kuijken, K., & Daddi, E. 2003, AJ, 125, 1107

Le Floc'h, E., Papovich, C., Dole, H., Bell, E. F., Lagache, G., Rieke, G. H., Egami, E., Pérez-González, P. G., Alonso-Herrero, A., Rieke, M. J., Blaylock, M., Engelbracht, C. W., Gordon, K. D., Hines, D. C., Misselt, K. A., Morrison, J. E., & Mould, J. 2005, ApJ, 632, 169

Lisker, T. 2008, ApJS, 179, 319

Lonsdale, C. J., Polletta, M. d. C., Omont, A., Shupe, D., Berta, S., Zylka, R., Siana, B., Lutz, D., Farrah, D., Smith, H. E., Lagache, G., DeBreuck, C., Owen, F., Beelen, A., Weedman, D., Franceschini, A., Clements, D., Tacconi, L., Afonso-Luis, A., Pérez-Fournon, I., Cox, P., & Bertoldi, F. 2009, ApJ, 692, 422

Lotz, J. M., Jonsson, P., Cox, T. J., & Primack, J. R. 2008, MNRAS, 391, 1137

—. 2009a, ArXiv e-prints

—. 2009b, ArXiv e-prints

Lotz, J. M., Madau, P., Giavalisco, M., Primack, J., & Ferguson, H. C. 2006, ApJ, 636, 592

Lotz, J. M., Primack, J., & Madau, P. 2004, AJ, 128, 163

Lutz, D., Yan, L., Armus, L., Helou, G., Tacconi, L. J., Genzel, R., & Baker, A. J. 2005, ApJ, 632, L13

Magnelli, B., Elbaz, D., Chary, R. R., Dickinson, M., Le Borgne, D., Frayer, D. T., & Willmer, C. N. A. 2009, A&A, 496, 57

Magorrian, J., Tremaine, S., Richstone, D., Bender, R., Bower, G., Dressler, A., Faber, S. M., Gebhardt, K., Green, R., Grillmair, C., Kormendy, J., & Lauer, T. 1998, AJ, 115, 2285

Melbourne, J., Bussman, R. S., Brand, K., Desai, V., Armus, L., Dey, A., Jannuzi, B. T., Houck, J. R., Matthews, K., & Soifer, B. T. 2009, AJ, 137, 4854

Melbourne, J., Desai, V., Armus, L., Dey, A., Brand, K., Thompson, D., Soifer, B. T., Matthews, K., Jannuzi, B. T., & Houck, J. R. 2008, AJ, 136, 1110

Menéndez-Delmestre, K., Blain, A. W., Smail, I., Alexander, D. M., Chapman, S. C., Armus, L., Frayer, D., Ivison, R. J., & Teplitz, H. 2009, ApJ, 699, 667

Mihos, J. C. & Hernquist, L. 1996, ApJ, 464, 641

Narayanan, D., Dey, A., Hayward, C., Cox, T. J., Bussmann, R. S., Brodwin, M., Jonsson, P., Hopkins, P., Groves, B., Younger, J. D., & Hernquist, L. 2009, ArXiv e-prints

Neugebauer, G., Habing, H. J., van Duinen, R., Aumann, H. H., Baud, B., Beichman, C. A., Beintema, D. A., Boggess, N., Clegg, P. E., de Jong, T., Emerson, J. P., Gautier, T. N., Gillett, F. C., Harris, S., Hauser, M. G., Houck, J. R., Jennings, R. E., Low, F. J., Marsden, P. L., Miley, G., Olnon, F. M., Pottasch, S. R., Raimond, E., Rowan-Robinson, M., Soifer, B. T., Walker, R. G., Wesselius, P. R., & Young, E. 1984, ApJ, 278, L1

Peng, C. Y., Ho, L. C., Impey, C. D., & Rix, H.-W. 2002, AJ, 124, 266

Petrosian, V. 1976, ApJ, 209, L1

Pierce, C. M., Lotz, J. M., Primack, J. R., Rosario, D. J. V., Griffith, R. L., Conselice, C. J., Faber, S. M., Koo, D. C., Coil, A. L., Salim, S., Koekemoer, A. M., Laird, E. S., Ivison, R. J., & Yan, R. 2010, MNRAS, 455

Polletta, M., Weedman, D., Hönig, S., Lonsdale, C. J., Smith, H. E., & Houck, J. 2008, ApJ, 675, 960

Rieke, G. H., Young, E. T., Engelbracht, C. W., Kelly, D. M., Low, F. J., Haller, E. E., Beeman, J. W., Gordon, K. D., Stansberry, J. A., Misselt, K. A., Cadien, J., Morrison, J. E., Rivlis, G., Latter, W. B., Noriega-Crespo, A., Padgett, D. L., Stapelfeldt, K. R., Hines, D. C., Egami, E., Muzerolle, J., Alonso-Herrero, A., Blaylock, M., Dole, H., Hinz, J. L., Le Floc'h, E., Papovich, C., Pérez-González, P. G., Smith, P. S., Su, K. Y. L., Bennett, L., Frayer, D. T., Henderson, D., Lu, N., Masci, F., Pesenson, M., Rebull, L., Rho, J., Keene, J., Stolovy, S., Wachter, S., Wheaton, W., Werner, M. W., & Richards, P. L. 2004, ApJS, 154, 25

Sajina, A., Yan, L., Armus, L., Choi, P., Fadda, D., Helou, G., & Spoon, H. 2007, ApJ, 664, 713

Sajina, A., Yan, L., Lutz, D., Steffen, A., Helou, G., Huynh, M., Frayer, D., Choi, P., Tacconi, L., & Dasyra, K. 2008, ApJ, 683, 659

Sanders, D. B. & Mirabel, I. F. 1996, ARA&A, 34, 749

Sanders, D. B., Soifer, B. T., Elias, J. H., Madore, B. F., Matthews, K., Neugebauer, G., & Scoville, N. Z. 1988a, ApJ, 325, 74

Sanders, D. B., Soifer, B. T., Elias, J. H., Neugebauer, G., & Matthews, K. 1988b, ApJ, 328, L35

Sargsyan, L. A., Weedman, D. W., & Houck, J. R. 2010, ApJ, 715, 986

Schade, D., Lilly, S. J., Crampton, D., Hammer, F., Le Fevre, O., & Tresse, L. 1995, ApJ, 451, L1+

Sersic, J. L. 1968, Atlas de galaxias australes (Cordoba, Argentina: Observatorio Astronomico, 1968)

Smail, I., Ivison, R. J., & Blain, A. W. 1997, ApJ, 490, L5+

Soifer, B. T., Sanders, D. B., Neugebauer, G., Danielson, G. E., Lonsdale, C. J., Madore, B. F., & Persson, S. E. 1986, ApJ, 303, L41

Swinbank, A. M., Chapman, S. C., Smail, I., Lindner, C., Borys, C., Blain, A. W., Ivison, R. J., & Lewis, G. F. 2006, MNRAS, 371, 465

Swinbank, A. M., Smail, I., Chapman, S. C., Borys, C., Alexander, D. M., Blain, A. W., Conselice, C. J., Hainline, L. J., & Ivison, R. J. 2010, MNRAS, 405, 234

Tacconi, L. J., Genzel, R., Smail, I., Neri, R., Chapman, S. C., Ivison, R. J., Blain, A., Cox, P., Omont, A., Bertoldi, F., Greve, T., Förster Schreiber, N. M., Genel, S., Lutz, D., Swinbank, A. M., Shapley, A. E., Erb, D. K., Cimatti, A., Daddi, E., & Baker, A. J. 2008, ApJ, 680, 246

Thompson, R. I., Rieke, M., Schneider, G., Hines, D. C., & Corbin, M. R. 1998, ApJ, 492, L95+

Trauger, J. T., Ballester, G. E., Burrows, C. J., Casertano, S., Clarke, J. T., Crisp, D., Evans, R. W., Gallagher, III, J. S., Griffiths, R. E., Hester, J. J., Hoessel, J. G., Holtzman, J. A., Krist, J. E., Mould, J. R., Scowen, P. A., Stapelfeldt, K. R., Watson, A. M., & Westphal, J. A. 1994, ApJ, 435, L3

Viana, A., Wiklind, T., Koekemoer, A., Thatte, D., Dahlen, T., Barker, E., de Jong, R., & Pirzkal, N. 2009, NICMOS Instrument Handbook Volume 11

Weedman, D., Polletta, M., Lonsdale, C. J., Wilkes, B. J., Siana, B., Houck, J. R., Surace, J., Shupe, D., Farrah, D., & Smith, H. E. 2006a, ApJ, 653, 101

Weedman, D. W., Soifer, B. T., Hao, L., Higdon, J. L., Higdon, S. J. U., Houck, J. R., Le Floc'h, E., Brown, M. J. I., Dey, A., Jannuzi, B. T., Rieke, M., Desai, V., Bian, C., Thompson, D., Armus, L., Teplitz, H., Eisenhardt, P., & Willner, S. P. 2006b, ApJ, 651, 101

Yan, L., Helou, G., Fadda, D., Marleau, F. R., Lacy, M., Wilson, G., Soifer, B. T., Drozdovsky, I., Masci, F., Armus, L., Teplitz, H. I., Frayer, D. T., Surace, J., Storrie-Lombardi, L. J., Appleton, P. N., Chapman, S., Choi, P., Fan, F., Heinrichsen, I., Im, M., Schmitz, M., Shupe, D. L., & Squires, G. K. 2004, ApJS, 154, 60

Yan, L., Sajina, A., Fadda, D., Choi, P., Armus, L., Helou, G., Teplitz, H., Frayer, D., & Surace, J. 2007, ApJ, 658, 778

Younger, J. D., Omont, A., Fiolet, N., Huang, J., Fazio, G. G., Lai, K., Polletta, M., Rigopoulou, D., & Zylka, R. 2009, MNRAS, 394, 1685

APPENDIX

A. IMAGES

In this section, we present postage stamp images and provide a brief qualitative description of each of the bump DOGs (as well as one DOG from the Cycle 16 *HST* imaging program that is a power-law source). Figure A1 shows $3'' \times 3''$ cutout images of the DOGs in order of increasing redshift (note that redshifts are not available for the first two sources presented). Each cutout is centered roughly on the centroid of emission as seen in the NICMOS image. A red plus sign shows the centroid of IRAC $3.6\mu m$ emission and is sized to represent the 1-σ uncertainty in the position, which includes independent contributions from the centroiding error on the $3.6\mu m$ emission ($\approx 0.''1$-$0.''3$, depending on S/N), the relative astrometric calibration uncertainty within the $3.6\mu m$ map ($\approx 0.''2$), and the uncertainty in tying the $3.6\mu m$ map to the *HST* images ($\approx 0.''1$). The 1σ rms offset between IRAC and NICMOS centroids of the sample is $0.''2$. In most cases, the offset in centroids is negligible, but those cases where it is not are associated with faint $3.6\mu m$ emission (when the absolute astrometric uncertainty may be as large as $0.''4$). This suggests there is no significant offset between the near-IR and mid-IR centroids at > 1 kpc scales.

The DOGs exhibit a wide range of morphologies, with most being well-resolved. Only one object (SST24 J143143.3+324944) shows strong Airy rings and is clearly an unresolved point source. However, we note that this source has a power-law dominated mid-IR SED and is not representative of the bump DOG population. Here we give a brief qualitative description of the morphology of each object.

(1) SST24 J143143.3+324944: F814W: Faint compact morphology. F160W: Bright, compact morphology; dominated by unresolved component.

(2) SST24 J143152.4+350029: F814W: Faint diffuse morphology. F160W: Bright, extended morphology; low surface brightness extension to southwest.

(3) SST24 J142724.9+350823: F814W: Faint, compact source $\approx 0.''5$ SW of NIC2 centroid. F160W: Bright, extended morphology with tentative evidence of tidal tails or spiral arms.

(4) SST24 J142951.1+342041: F814W: Faint, compact source $\approx 0.''3$ north of NIC2 centroid. F160W: Bright, clumpy morphology.

(5) SST24 J143216.8+335231: F814W: Faint, compact source at eastern edge of NIC2 emission. F160W: Bright, clumpy morphology; two bad pixels within the segmentation map of this galaxy have been masked out in the analysis.

(6) SST24 J143137.1+334500: F814W: No detection. F160W: Extended narrow morphology resembling a giant edge-on disk with semi-major axis larger than $3''$.

(7) SST24 J142832.4+340850: F814W: Faint, compact morphology. F160W: No usable data.

(8) SST24 J143816.6+333700: F814W: Faint, compact morphology. F160W: Bright, compact morphology; no obvious PSF signature.

(9) SST24 J143349.5+334602: F814W: Faint, clumpy morphology. F160W: Two distinct faint, compact sources; IRAC centroid is closer to eastern source.

(10) SST24 J143020.4+330344: F814W: No detection. F160W: Compact morphology; no obvious PSF signature.

(11) SST24 J142652.4+345504: F814W: No detection. F160W: Two faint sources separated by $\approx 2''$; IRAC centroid consistent with northeastern source.

(12) SST24 J142941.0+340915: F814W: No detection. F160W: Clumpy morphology.

(13) SST24 J143324.2+334239: F814W: Faint, compact morphology. F160W: Bright, compact morphology; low surface brightness extension to southwest.

(14) SST24 J143331.9+352027: F814W: Very faint, clumpy morphology. F160W: Bright, clumpy morphology; low surface brightness extension to northeast.

(15) SST24 J143503.3+340243: F814W: No detection. F160W: Bright, compact morphology; no obvious PSF signature.

(16) SST24 J142920.1+333023: F814W: Faint, compact morphology. F160W: Bright, compact morphology.

(17) SST24 J143321.8+342502: F814W: Faint, compact source spatially coincident with peak NIC2 emission. F160W: Bright, compact morphology; no obvious PSF signature; strong low surface brightness feature extending northeast.

(18) SST24 J143502.9+342657: F814W: No detection. F160W: Very clumpy morphology with low surface brightness feature extending to south.

(19) SST24 J143458.8+333437: F814W: Very faint, compact morphology. F160W: Bright, compact morphology; low surface brightness feature to northwest resembles a tidal tail.

(20) SST24 J143028.5+343221: F814W: Very faint, clumpy morphology. F160W: Bright, clumpy morphology; low surface brightness features extending in eastern and southern directions.

(21) SST24 J143702.0+344631: F814W: No detection. F160W: No detection.

(22) SST24 J142637.3+333025: F814W: Faint compact morphology. F160W: Faint compact morphology; formally detected at 3σ level with $0\farcs6$ diameter aperture.

B. SMG AND XFLS ULIRG NON-PARAMETRIC MORPHOLOGIES

The morphologies presented herein comprise a large sample of high redshift ULIRGs analyzed in a uniform manner. This minimizes systematic uncertainties in the morphological measurements by facilitating interpretation of the results in a relative sense.

Table B2 presents the measurements of non-parametric morphologies of SMGs at $z > 1.4$ derived from NIC2 images using the same morphology code used to analyze the imaging of XFLS ULIRGs and DOGs. A total of 18 SMGs meet this requirement, but 2 of these have per-pixel-S/N< 2 and are not included in our analysis here. This table also includes an estimate of whether the source is dominated by a bump or by a power-law in the mid-IR using IRAC data from Hainline et al. (2009) and the same statistical definition originally used for DOGs (Dey et al. 2008).

Swinbank et al. (2010) present measurements of $r_{\rm P}$ and G for SMGs, and it is instructive to compare their results with ours here. We find that our size measurements are generally consistent, with median $r_{\rm P}$ values of 8.4 kpc in our analysis and 8.6 kpc in that of Swinbank et al. (2010). We also find no systematic offset either at large or small radii in the $r_{\rm P}$ values.

On the other hand, we find significant offsets in the respective measurements of G. Our median G value for SMGs at $z > 1.4$ is 0.49, while that of Swinbank et al. (2010) is 0.54. Additionally, aside from a few exceptions, there is tentative evidence that the offset increases with S/N-per-pixel. These offsets may be the result of a different means of selecting which pixels belong to the galaxy in question. As discussed in section 3.2.2, pixels with surface brightness above $\mu(r_{\rm P})$ are assigned to the galaxy while those below it are not. Meanwhile, Swinbank et al. (2010) adopt $1.5r_{\rm P}$ as their Petrosian radius. Studies of the morphologies of galaxies in the *HST* Ultra-deep field (UDF) have shown that the G coefficient has a strong dependence on the specific definition used for the Petrosian radius (Lisker 2008). At reliable S/N levels (S/N> 2), Lisker (2008) show that using the larger aperture to define a galaxy's extent can cause an increase in G of up to 0.1, with some evidence for an increase in the offset with S/N. This effect is thus qualitatively consistent with the differences observed between our measurements and those presented in Swinbank et al. (2010).

The primary takeaway of this comparison is that when comparing morphologies of objects, it is necessary to apply a single systematic method in analyzing all objects in the sample. We note that the central conclusions presented in Swinbank et al. (2010) are based on measurements of the morphologies of SMGs relative to a population of field galaxies and are therefore robust.

Finally, Table B3 presents our measurements of non-parametric morphologies of XFLS ULIRGs at $z > 1.4$ derived from NIC2 images using the same morphology code used to analyze the imaging of SMGs and DOGs.
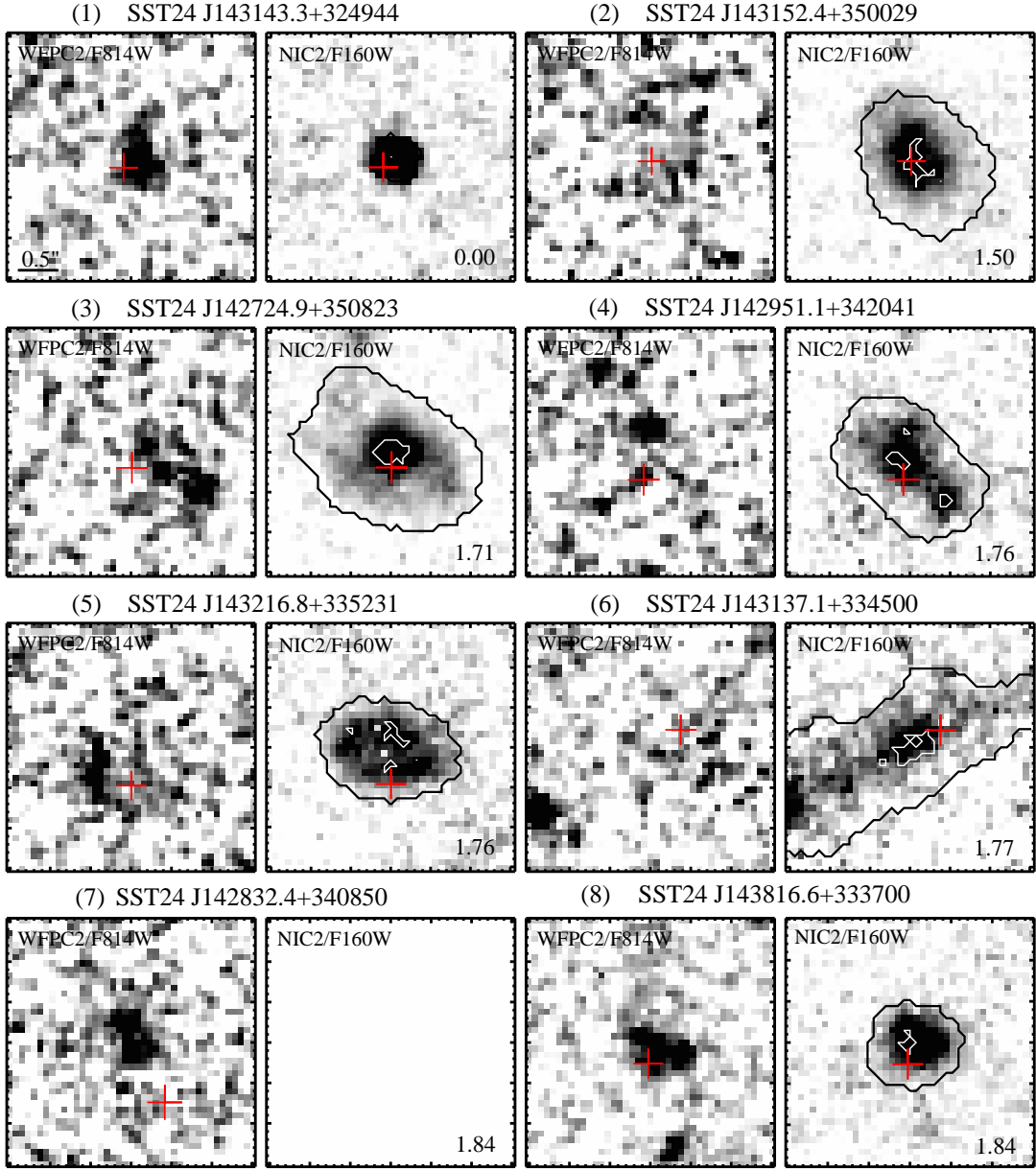
FIG. A1.— Cutouts of the 22 DOGs observed by *HST*, shown with a linear stretch. Columns 1 and 3 are the rest-UV images from WFPC2 F814W and columns 2 and 4 are the rest-optical images from NIC2 F160W. Each cutout is $3''$ on a side and is oriented north up and east left. The objects are arranged in order of increasing redshift, and the redshift is printed in the lower right corner of each NICMOS image. A red cross denotes the position and 1-σ uncertainty in the centroid of the IRAC 3.6μm emission. In images where the S/N per pixel is greater than 2, white contours outline the brightest 20% pixels (for computing M_{20}), and black contours show the outline of the segmentation map used in measuring the non-parametric morphologies. NICMOS imaging is not available for target SST24 J142832.4+340850.

(9)   SST24 J143349.5+334602   (10)   SST24 J143020.4+330344

(11)   SST24 J142652.4+345504   (12)   SST24 J142941.0+340915

(13)   SST24 J143324.2+334239   (14)   SST24 J143331.9+352027

(15)   SST24 J143503.3+340243   (16)   SST24 J142920.1+333023

FIG. A1.— Continued.

(17) SST24 J143321.8+342502

(18) SST24 J143502.9+342657

(19) SST24 J143458.8+333437

(20) SST24 J143028.5+343221

(21) SST24 J143702.0+344631
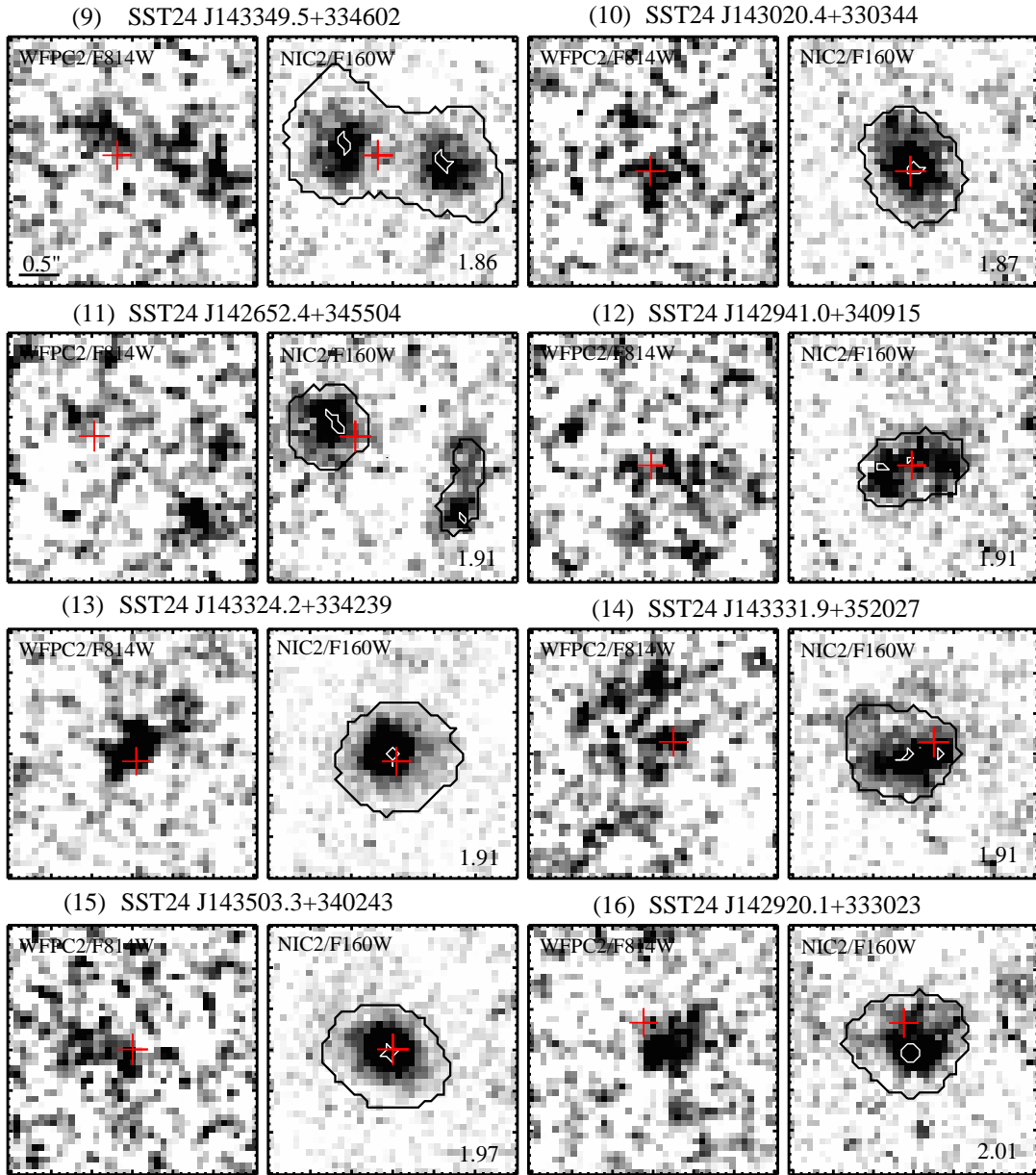
(22) SST24 J142637.3+333025
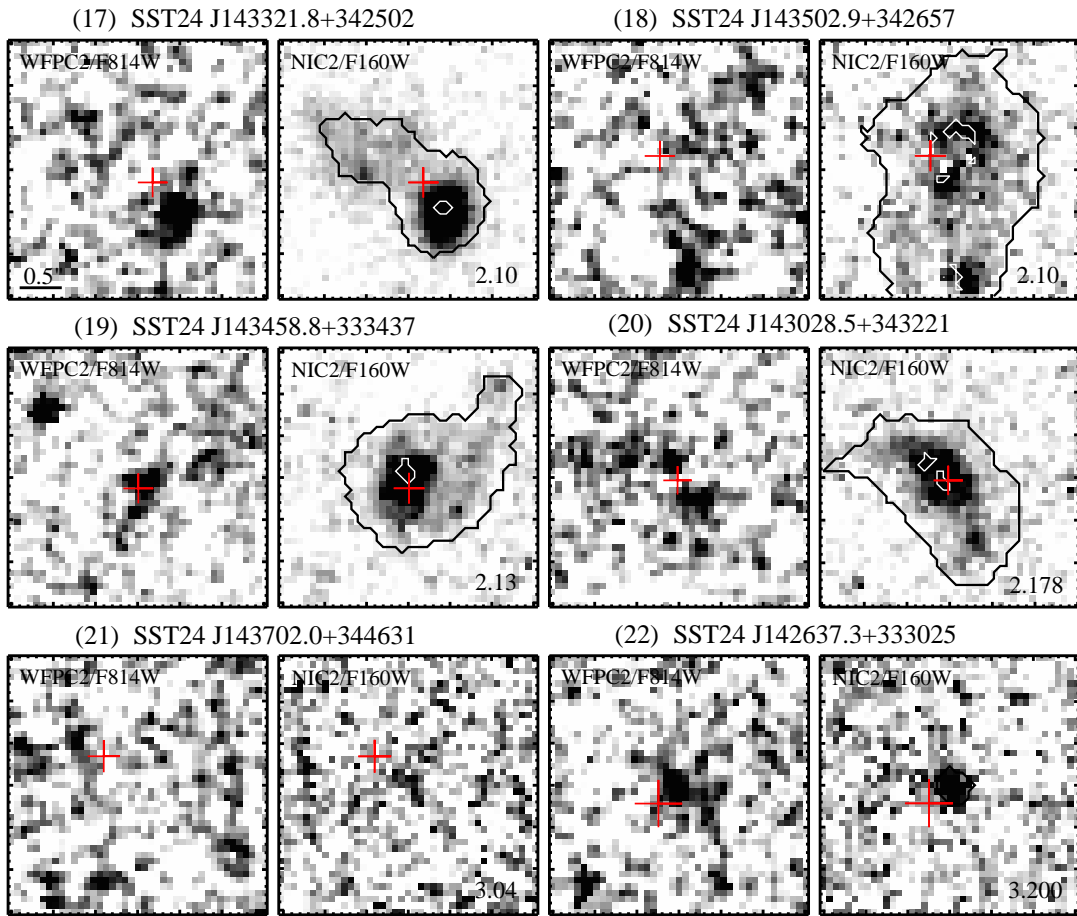
FIG. A1.— Continued.

TABLE B1
NICMOS Morphological Classifications

Source Name	SED	Visual[a]	$N_{\rm agr}$[b]	S/N	$r_{\rm P}$ (kpc)	G	M_{20}	C	PSF Fraction	$R_{\rm eff}$ (kpc)	n	Axial Ratio	$N_{\rm dof}$	χ^2_ν
SST24 J142637.3+333025	PL	TFTT	4	3.1	2.3±1.0	0.47±0.03	-1.72±0.10	2.9±0.4	0.45±0.55	—	0.1±1.7	0.15±0.49	1594	2.3
SST24 J142652.4+345504	Bump	Reg	4	3.8	8.6±0.9	0.38±0.03	-0.77±0.10	3.4±0.4	0.11±0.20	3.3±0.4	1.1±0.2	0.84±0.06	1654	1.6
SST24 J142724.9+350823	Bump	Irr	6	4.1	12.0±0.8	0.48±0.03	-1.63±0.10	4.9±0.4	0.04±0.06	4.6±0.2	1.5±0.1	0.69±0.02	1656	1.1
SST24 J142832.4+340850	Bump	—	—	—	—	—	—	—	—	–	—	—	—	—
SST24 J142920.1+333023	Bump	Irr	6	3.4	6.9±1.0	0.48±0.03	-1.00±0.10	2.8±0.4	0.08±0.09	3.3±0.2	0.8±0.1	0.79±0.04	1663	2.5
SST24 J142941.0+340915	Bump	Irr	7	2.8	6.6±1.2	0.40±0.04	-0.99±0.11	1.7±0.5	0.07±0.18	3.9±1.8	0.0±0.1	0.57±0.04	1635	2.1
SST24 J142951.1+342041	Bump	Irr	6	4.0	10.7±0.8	0.46±0.03	-0.98±0.10	2.8±0.4	0.03±0.09	5.2±0.1	0.3±0.1	0.42±0.01	1668	3.2
SST24 J143020.4+330344	Bump	Reg	7	3.3	7.0±1.0	0.49±0.03	-1.63±0.10	3.0±0.4	0.13±0.11	2.9±0.2	0.9±0.2	0.64±0.04	1599	3.4
SST24 J143028.5+343221	PL	Irr	6	2.5	9.7±1.3	0.51±0.05	-1.18±0.13	4.0±0.5	0.05±0.05	4.4±0.2	0.7±0.1	0.39±0.02	1639	2.8
SST24 J143137.1+334500	Bump	Irr	4	2.5	27.5±1.3	0.44±0.05	-1.00±0.13	3.2±0.5	0.10±0.13	10.5±0.8	0.7±0.1	0.26±0.01	1657	1.1
SST24 J143143.3+324944	PL	Reg	7	11.3	0.0±0.0	0.52±0.02	-1.69±0.06	3.0±0.3	0.42±0.05	—	1.0±0.4	0.66±0.03	1665	2.7
SST24 J143152.4+333029	Bump	Irr	4	5.2	8.9±0.8	0.46±0.03	-1.41±0.06	4.8±0.4	0.02±0.03	3.9±0.1	0.7±0.1	0.69±0.01	1666	2.2
SST24 J143216.8+335231	Bump	Irr	4	4.4	8.4±0.8	0.38±0.03	-0.98±0.08	2.4±0.4	0.00±0.08	4.2±0.1	0.1±0.1	0.60±0.01	1666	2.0
SST24 J143321.8+342502	Bump	Irr	6	5.0	8.2±0.8	0.54±0.03	-0.78±0.06	3.3±0.4	0.13±0.05	1.8±0.1	1.4±0.1	0.61±0.02	1659	1.6
SST24 J143324.2+334239	Bump	Reg	7	3.8	6.7±0.9	0.54±0.03	-1.62±0.10	3.0±0.4	0.12±0.06	2.6±0.1	1.2±0.1	0.80±0.03	1612	2.6
SST24 J143331.9+352027	Bump	Irr	6	4.1	8.2±0.8	0.37±0.03	-0.85±0.09	2.4±0.4	0.00±0.08	4.7±0.2	0.9±0.1	0.57±0.03	1658	2.7
SST24 J143349.5+334602	Bump	Irr	7	2.5	11.8±1.3	0.48±0.05	-0.83±0.12	1.9±0.5	0.05±0.07	3.2±0.3	0.8±0.1	0.67±0.04	1660	2.4
SST24 J143458.8+333437	Bump	Irr	7	2.5	9.6±1.3	0.54±0.05	-1.24±0.12	3.8±0.5	0.15±0.10	4.9±0.5	2.1±0.3	0.81±0.03	1657	1.9
SST24 J143502.9+342657	Bump	Irr	7	2.1	14.9±1.5	0.46±0.05	-0.77±0.15	2.4±0.6	0.03±0.25	8.8±3.5	0.0±0.1	0.35±0.02	1669	1.3
SST24 J143503.3+340243	Bump	Reg	6	4.0	7.2±0.8	0.53±0.03	-1.71±0.10	2.8±0.4	0.09±0.09	2.9±0.1	1.0±0.1	0.62±0.02	1659	1.8
SST24 J143702.0+344631	Bump	TFTT	7	—	—	—	—	—	—	—	—	–	—	—
SST24 J143816.6+333700	Bump	Reg	5	5.1	5.7±0.8	0.47±0.03	-1.47±0.06	2.6±0.4	0.06±0.04	2.3±0.1	0.4±0.1	0.81±0.02	1666	1.9

[a] Mode of visual classification.

[b] Number of users in agreement with mode of visual classification.

Source Name	SED	S/N	r_P (kpc)	G	M_{20}	C	PSF Fraction	R_{eff} (kpc)	n	N_{dof}	χ^2_ν
CFRS03-15	Bump	6.1	12.5±0.8	0.57±0.02	-1.72±0.06	4.3±0.3	0.00± 0.02	40.7±34.1	18.3±3.8	1671	4.3
LOCKMAN-03	Bump	4.4	13.4±0.8	0.51±0.03	-1.15±0.08	3.0±0.4	0.00± 0.03	4.5± 0.2	1.2±0.1	1671	1.4
LOCKMAN-06	Bump	3.5	10.2±0.9	0.48±0.03	-1.46±0.10	3.0±0.4	0.00± 0.05	5.3± 0.4	2.0±0.1	1671	0.9
LOCKMAN-02	Bump	4.0	12.9±0.8	0.46±0.03	-0.99±0.10	4.5±0.4	0.03± 0.07	5.4± 0.1	0.5±0.0	1663	0.7
HDFN-082	Bump	< 2	—	—	—	—	—	—	—	—	—
HDFN-092	Bump	2.0	8.2±1.4	0.45±0.05	-0.96±0.15	5.4±0.6	0.11± 0.16	4.1± 0.1	0.1±0.1	1671	1.2
HDFN-093	Bump	5.8	3.4±0.8	0.49±0.02	-1.76±0.06	3.2±0.3	0.19± 0.03	1.3± 0.2	4.2±1.2	1664	0.7
HDFN-105	Bump	7.1	4.8±0.7	0.49±0.02	-1.73±0.06	2.8±0.3	0.00± 0.08	2.5± 0.2	2.9±0.2	1671	1.4
HDFN-127	PL	3.1	4.6±1.0	0.49±0.03	-1.17±0.10	3.5±0.4	0.41± 0.21	1.7± 0.2	0.2±0.2	1671	1.4
HDFN-143	Bump	3.4	8.4±1.0	0.34±0.03	-1.04±0.10	2.4±0.4	0.02± 0.08	4.4± 0.1	0.2±0.1	1670	0.7
HDFN-161	Bump	5.5	5.4±0.8	0.58±0.03	-1.80±0.06	3.4±0.3	0.01± 0.10	29.8±41.9	20.0±7.6	1671	1.9
HDFN-172	Bump	5.5	8.6±0.8	0.46±0.03	-1.02±0.06	2.4±0.3	0.18± 0.09	4.1± 0.3	1.7±0.2	1671	1.7
SA13-332	PL	5.1	3.2±0.7	0.51±0.03	-1.62±0.06	3.0±0.4	0.47± 0.03	1.4± 0.1	0.9±0.3	1666	0.6
SA13-570	PL	3.2	7.0±1.0	0.49±0.03	-1.76±0.10	2.7±0.4	0.03± 0.18	2.9± 0.1	1.5±0.2	1662	0.5
CFRS14-3	Bump	5.7	6.1±0.8	0.59±0.02	-1.56±0.06	3.4±0.3	0.01± 0.09	1.6± 0.1	3.4±0.3	1671	1.4
ELAIS-13	Bump	< 2	—	—	—	—	—	—	—	—	—
ELAIS-07	Bump	4.7	8.6±0.8	0.46±0.03	-0.96±0.07	4.3±0.4	0.00± 0.08	3.7± 0.2	1.4±0.1	1671	1.5
ELAIS-04	Bump	5.6	9.3±0.8	0.54±0.03	-1.30±0.06	3.8±0.3	0.05± 0.04	3.3± 0.0	0.5±0.0	1671	3.3

TABLE B3
XFLS NICMOS Morphological Classifications

Source Name	SED	S/N	r_P (kpc)	G	M_{20}	C	PSF Fraction	R_{eff} (kpc)	n	N_{dof}	χ^2_ν
MIPS506	Bump	5.0	5.2±0.8	0.46±0.02	-1.45±0.06	3.1±0.3	0.15±0.24	2.6±0.2	1.3±0.1	1671	0.8
MIPS289	Bump	5.2	11.1±0.8	0.54±0.02	-2.01±0.06	3.4±0.3	0.08±0.03	4.7±0.3	2.2±0.2	1671	2.1
MIPS8342	Bump	8.0	5.3±0.8	0.57±0.03	-1.73±0.10	3.1±0.4	0.11±0.04	1.3±0.1	2.1±0.1	1671	1.2
MIPS8242	Bump	4.7	12.8±0.9	0.44±0.03	-0.89±0.10	3.3±0.4	0.05±0.04	5.4±0.1	0.5±0.1	1671	2.1
MIPS464	PL	5.2	4.6±0.8	0.40±0.03	-1.59±0.06	2.5±0.4	0.16±0.70	1.9±0.1	0.7±0.1	1671	1.0
MIPS227	Bump	10.4	7.7±1.3	0.54±0.05	-1.84±0.13	3.0±0.5	0.03±0.01	2.6±0.1	1.6±0.1	1671	1.7
MIPS8196	Bump	8.5	9.0±0.7	0.54±0.02	-2.09±0.06	3.7±0.3	0.07±0.01	4.4±0.2	4.0±0.2	1671	1.8
MIPS8327	Bump	5.9	5.6±0.9	0.51±0.03	-1.44±0.10	2.8±0.4	0.00±0.06	1.8±0.1	3.4±0.4	1671	1.4
MIPS8245	Bump	3.2	3.5±0.8	0.44±0.03	-0.96±0.06	2.2±0.4	0.00±1.00	1.6±0.1	0.4±0.2	1670	1.7
MIPS78	PL	2.2	6.5±0.8	0.43±0.03	-0.84±0.06	2.5±0.4	0.21±0.51	2.7±0.3	0.3±0.1	1671	1.5
MIPS180	Bump	4.7	3.6±0.8	0.41±0.02	-1.90±0.06	2.4±0.3	0.31±0.82	1.6±0.1	0.2±0.2	1671	1.8
MIPS42	PL	3.4	5.2±0.8	0.47±0.02	-0.95±0.06	2.5±0.3	0.14±0.18	2.2±0.3	1.1±0.5	1671	2.0
MIPS8493	Bump	3.7	12.1±1.5	0.49±0.05	-1.09±0.15	3.7±0.6	0.00±0.07	5.3±0.3	1.2±0.1	1671	1.3
MIPS22661	Bump	8.1	4.8±0.8	0.50±0.03	-1.81±0.06	2.9±0.4	0.21±0.04	1.8±0.1	1.0±0.1	1670	2.4
MIPS22277	Bump	7.8	5.9±0.8	0.53±0.02	-1.67±0.06	3.0±0.3	0.06±0.03	2.0±0.1	2.0±0.1	1670	1.4
MIPS22204	PL	11.6	3.4±1.0	0.51±0.03	-1.60±0.10	2.9±0.4	0.17±0.04	0.7±0.1	3.7±0.3	1671	1.5
MIPS16080	Bump	5.5	9.4±0.8	0.57±0.03	-1.39±0.06	3.5±0.3	0.03±0.03	2.8±0.1	2.8±0.2	1671	1.4
MIPS22303	PL	2.4	6.4±0.8	0.42±0.02	-0.99±0.06	2.6±0.3	0.19±0.29	2.6±0.5	1.1±0.3	1669	1.0
MIPS15977	Bump	8.6	5.8±1.4	0.52±0.05	-1.87±0.13	3.0±0.5	0.22±0.04	2.5±0.1	0.7±0.1	1669	1.4
MIPS15928	Bump	7.7	7.5±0.7	0.52±0.02	-1.90±0.06	3.1±0.3	0.22±0.05	3.2±0.1	0.6±0.1	1671	2.8
MIPS15840	PL	4.4	4.8±0.8	0.45±0.03	-1.47±0.10	2.8±0.4	0.18±0.22	2.2±0.1	0.6±0.1	1671	1.1
MIPS22651	Bump	6.0	7.7±1.4	0.58±0.05	-2.00±0.14	3.3±0.6	0.11±0.06	2.4±0.1	1.6±0.1	1671	1.2
MIPS22558	Bump	4.8	3.6±0.8	0.51±0.03	-1.84±0.07	3.4±0.4	0.16±0.12	3.1±2.2	10.9±5.2	1671	0.8
MIPS22699	PL	4.3	3.6±1.3	0.49±0.05	-2.37±0.13	3.0±0.5	0.09±1.00	0.9±0.1	3.2±0.9	1671	1.1
MIPS16122	PL	2.4	7.6±0.7	0.46±0.02	-1.26±0.06	3.0±0.3	0.04±0.20	2.3±0.1	1.2±0.1	1671	1.6
MIPS15949	Bump	4.0	8.6±0.7	0.61±0.02	-1.52±0.06	3.7±0.3	0.28±0.05	2.8±0.2	1.7±0.2	1671	1.0
MIPS15880	Bump	4.0	8.8±1.0	0.46±0.03	-1.08±0.10	2.3±0.4	0.03±0.08	5.4±0.3	0.7±0.1	1671	1.8
MIPS16113	Bump	1.6	9.0±0.8	0.47±0.03	-0.66±0.09	1.8±0.4	0.02±0.12	2.6±0.2	1.5±0.2	1671	1.6
MIPS22530	Bump	2.4	10.0±0.8	0.47±0.03	-1.42±0.07	2.5±0.4	0.03±0.13	3.9±0.3	0.9±0.1	1664	1.5
MIPS15958	PL	7.7	3.7±0.8	0.53±0.03	-1.74±0.08	3.0±0.4	0.67±0.10	1.6±0.1	0.4±0.1	1671	1.1
MIPS16095	Bump	9.3	5.7±0.8	0.52±0.02	-1.83±0.06	3.1±0.3	0.06±0.04	1.9±0.1	1.7±0.1	1671	1.2
MIPS16144	Bump	3.7	13.0±0.8	0.50±0.02	-1.46±0.06	4.4±0.3	0.10±0.04	5.6±1.0	3.1±0.6	1664	1.3
MIPS16059	Bump	5.2	8.4±0.8	0.53±0.02	-1.31±0.06	2.5±0.3	0.05±0.05	2.9±0.1	0.3±0.1	1671	1.7